

- 26 DUBOST G., NICOLAS, M., VALLEE, P.: 'Antenne à pas de balayage réduit dans un large secteur angulaire'. Brevet 8507 348, 15 May 1985
- 27 DUBOST, G.: 'Antenne à symétrie de révolution associant une lentille diélectrique à une source plaque'. IEEE Symposium AP-S, Vancouver, Canada, June 1985, pp. 587-590
- 28 DUBOST, G.: 'Flat linear radiating array applied on a cylindrical lens'. Melecon '85 Mediterranean Electrotechnical Conference, Madrid, Oct. 1985, pp. 215-218
- 29 DUBOST, G.: 'Short-or open-circuited dipole parallel to perfect reflector plane and embedded in substrate and acting at resonance', *Electron. Lett.*, 1981, 17, pp. 914-916
- 30 DUBOST, G.: 'Transmission-line model analysis of a lossy rectangular microstrip patch' *Electron. Lett.* 1982, 18, pp. 282-282
- 31 DUBOST, G., and RABBAA, A.: 'Mutual impedance between two short-circuited flat resonant dipoles', *IEEE Trans.*, 1981, AP-29, pp. 668-671
- 32 DUBOST, G.: 'Far field radiated by short-circuited microstrip antenna acting at a quarter wavelength resonance' *Electron. Lett.* 1983, 19, pp. 737-739
- 33 DUBOST, G., GUEHO, S., and BEGUIN, D.: 'Ku band phased array in a large angular sector', 5th Int. Conf. on Antennas and Propag., ICAP 87, 1987, University of York
- 34 DUBOST, G., and GUEHO, S.: 'A 3 bits digital phase shifter in Ku band for microstrip phased array'. 8th Colloquium on Microwave communication, Aug. 1986, Budapest, Hungary
- 35 DUBOST, G., GUEHO, S., BEGUIN, D.: 'Déphaseur élémentaire en ligne microruban et déphaseur à commande numérique en faisant application', Brevet 86 11 923, 21 Aug. 1986
- 36 DUBOST, G., GUEHO, S., and BEGUIN, D.: 'Antenne réseau carré, monopulse à balayage électronique'. Brevet 87 20774, 13 Jun. 1987
- 37 DUBOST, G., ALEXIS, R.: 'Antenne formée à partir d'une cavité résonnante comportant une face rayonnante'. Brevet 8408.392, 19 May 1984
- 38 DUBOST, G.: 'Antennes plaques pour les télécommunications entre stations mobiles' *L'Onde Electrique*, 1985), 65, pp. 41-49
- 39 DUBOST, G.: 'Vertically polarized flat antenna with omnidirectional radiation'. Int. Symposium on Antennas and Propagation, ISAP, Aug. 1985, Kyoto, Japan, pp. 109-112
- 40 DUBOST, G.: 'Influence of feed-point location on radiation resistance of a short-circuited flat dipole', *Electron. Lett.*, 1984, 20, pp. 980-981
- 41 DUBOST, G., BIZOUARD, A.: 'Antenne périodique plane'. Brevet 83.19.924 13 Dec. 1983
- 42 DUBOST, G., GUEHO, S., and BIZOUARD, A.: 'Log-periodic short-circuited dipole array with a squinted beam', *Electron. Lett.*, 20, pp. 411-413
- 43 DUBOST, G., and GUEHO, S.: 'Theory of a large bandwidth microstrip plane array with a deflected beam'. IEEE Int. Symposium on Ant. Prop., June 1984, Boston, Mass., USA

## Numerical analysis of microstrip patch antennas

J.R. Mosig, R.C. Hall and F.E. Gardiol

### 8.1 Introduction

#### 8.1.1 General description

Microstrip patch antennas are thin and lightweight radiating elements, formed by a substrate, including one or several dielectric layers, backed by a metallic sheet (the ground plane).

Thin metallic patches (the radiating elements) are located on the air-substrate interface and, possibly, between the dielectric layers. Microstrip antennas are manufactured by the photolithographic process developed for printed circuits. Their low profile, low weight and mechanical ruggedness make them an ideal choice for aerospace applications. They can be mass-produced, and could thus provide inexpensive receiver antennas for direct reception of microwave signals from satellites (television, mobile communications). Finally, they are ideally suited to be combined in large arrays, the individual patches sharing the same substrate. Thus directive antennas can be obtained in spite of the inherent low directivity of a single patch.

The remarkable practical advantages offered by microstrip antennas are offset, to some extent, by their inhomogeneous nature, and a rigorous analysis was long considered to be a hopeless task.

An accurate model should take into account the three inhomogeneities of a microstrip structure (Fig. 8.1):

- (a) The presence of at least two dielectrics (often air and substrate)
- (b) The boundary conditions on the interfaces between different layers are inhomogeneous since thin metallic plates making up the radiating elements and feeding the structure can partially fill the interfaces
- (c) Any microstrip structure is finite in dimensions; i.e. its ground plane and its dielectric substrate are bounded in the transverse directions. The edges may, however, be located at a very large distance, in which case this third inhomogeneity may be neglected (the structure is then assumed, mathematically, to extend to infinity).

Models used to study microstrip patch antennas range from very simplified ones, such as the transmission-line model, through cavity models, planar circuit analysis, segmentation techniques, and up to quite sophisticated approaches based on an integral-equation formulation. In the framework of the integral-equation model, many different approaches exist, depending on the use of spectral or space quantities and on the geometries to be included.

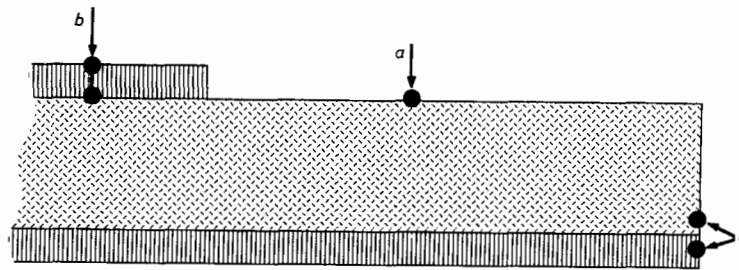


Fig. 8.1 The three inhomogeneities of a microstrip structure.  
 a Dielectric media of unequal permittivity,  
 b Infinitely thin conductors introducing surface current between the dielectric media  
 c Finite transverse dimensions of substrate and ground plane

Detailed surveys of these models are available (e.g. Reference 1), and several of them are treated elsewhere in this book.

### 8.1.2 The integral equation model

The purpose of this Chapter is to provide a rigorous treatment of microstrip antennas, free from over-simplifying assumptions. Among its principal features, the proposed model is able to handle patches of arbitrary shapes where no educated guess of the surface-current distribution is possible. Also there is no limitation in frequency and substrate thickness. The model automatically takes into account mutual coupling between elements and can predict the performance of a patch embedded in an array environment. Surface waves are included as well as dielectric and ohmic losses. Thus the model allows accurate prediction of quasistatic behaviour, dominant and higher modes of resonance, and input impedances, coupling coefficients, radiation patterns, gain and efficiency at any frequency.

The model relies upon the identification of a microstrip antenna as a particular case of a stratified medium. The pioneer work on electromagnetic-wave propagation in stratified media must be ascribed to A. Sommerfeld, who investigated the radio-wave propagation above a lossy ground as early as 1909.

The microstrip antenna is modelled by an integral equation where the main unknown is the electric surface current density on the patches. The Green's functions forming the kernel of this equation include the effects of the layers, and are obtained in the form of inverse Hankel transforms by the systematic use

of stratified media theory. The first Sections of this Chapter are devoted to the construction of the integral equation and of the pertinent Green's functions. Considerable attention is paid to the development of efficient numerical techniques for evaluating the Green's functions.

The integral equation is directly formulated in the space domain using a vector and a scalar potential. The resulting mixed potential integral equation (MPIE), similar to that obtained for wire antennas, is better suited for numerical analysis than the customary electric-field integral formulation.

The MPIE is solved by a method of moments. In the general case, rooftop subsectional-basis functions are used. For particular geometries, it can be more efficient to use entire domain-basis functions corresponding to the eigenvalues of the equivalent cavity. Finally, standard circuit analysis is used to deal with multiport antennas, loaded antennas and arrays.

The final Sections of the Chapter present numerical results for the input impedance, coupling coefficients and radiation patterns of several microstrip antennas and arrays of practical interest.

## 8.2 Model based on the electric surface current

### 8.2.1 Geometry of the model and boundary conditions

In order to present the theory in the clearest possible manner, the electric surface-current model will be developed for the simple microstrip structure of Fig. 8.2 with a single dielectric layer and a metallic patch. The generalisation to multilayer antennas and to multiple patches (arrays) will be considered later.

The substrate is assumed to extend to infinity in the transverse directions and is made of a nonmagnetic, isotropic, homogeneous material which can be lossy. The ground plane also has infinite dimensions, and the upper conductor (the metallic patch) has zero thickness. Both the ground plane and patch are allowed to have ohmic losses.

The direction perpendicular to the ground plane is selected as the  $z$ -axis (Fig. 8.2). The patch extends over part of the  $z = 0$  plane, denoted by the surface  $S_0$ . The remainder of the  $z = 0$  plane, i.e. the surface separating the two dielectric media, is denoted  $S$  and called hereinafter the interface.

Indexes 1 and 2 are associated, respectively, with the infinite dielectric extending above the substrate, usually the air, and with the substrate itself. Thus, we have

$$\epsilon_1 = \epsilon_0, \quad z > 0 \quad (8.1)$$

$$\epsilon_2 = \epsilon_0 \epsilon_r = \epsilon_0 \epsilon_r' (1 - j \tan \delta) \quad -h < z < 0$$

where  $h$  is the substrate thickness and

$$\mu_1 = \mu_2 = \mu_0 \quad (8.2)$$

everywhere.

The excitation is provided by a time-harmonic electromagnetic field. Complex phasor notation is used throughout this Chapter. Any complex scalar quantity  $C$  represents an instantaneous quantity  $C(t)$  given by:

$$C(t) = \sqrt{2} \operatorname{Re}[C \exp(j\omega t)] \quad (8.3)$$

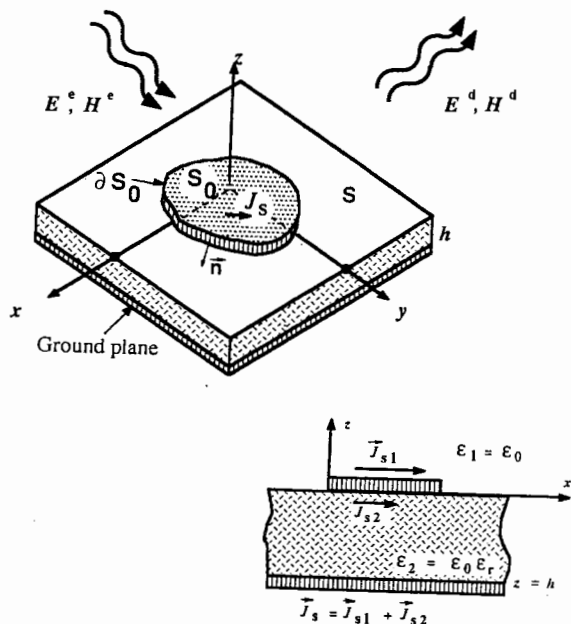


Fig. 8.2 General view of a microstrip antenna and vertical cut in the  $y = 0$  plane. Superscripts  $e$  and  $d$  refer to the incident fields (excitation) and to the scattered (diffracted) fields. For a infinitely thin patch the currents  $J_{s1}$  and  $J_{s2}$  can no longer be distinguished and the meaningful quantity is the total current  $J_s = J_{s1} + J_{s2}$  flowing on the patch.

The excitation fields are denoted by  $E^e$  and  $H^e$ . They can be the fields of a plane wave coming from infinity (receiving antenna) or the local fields created by a finite source located within the microstrip structure (transmitting antenna).

In either case, the excitation fields induce surface currents on the upper side of the ground plane and on both sides of the metallic patch. However, since the patch is assumed to have zero thickness, the model cannot differentiate between the currents flowing on its upper and lower side. Indeed, the patch is modelled as a sheet of current  $J_s$  whose value at any point is the algebraic sum of the upper and lower surface currents  $J_{s1}$  and  $J_{s2}$  existing at  $z = 0^+$  and  $z = 0^-$  (Fig. 8.2).

The induced currents in turn create diffracted or scattered electromagnetic fields. These fields, denoted  $E^d$ ,  $H^d$ , add to the excitation fields to yield the total fields  $E$ ,  $H$  existing in the entire space.

On the air-dielectric interface (the plane  $z = 0$ , excluding the surface of the patch  $S_0$ ) the boundary conditions are:

$$e_z \times (E_1 - E_2) = 0 \quad (8.4)$$

$$e_z \times (H_1 - H_2) = 0 \quad (8.5)$$

On the metallic surfaces the boundary conditions will be inhomogeneous owing to the presence of the currents. Assuming that the patch and the ground plane are perfect conductors (this restriction will be removed later) we have on the upper side of the patch  $S_0(z = 0^+)$ :

$$e_z \times E_1 = 0; \quad e_z \times H_1 = J_{s1} \quad (8.6)$$

and, similarly on the lower side  $z = 0^-$ :

$$e_z \times E_2 = 0; \quad e_z \times H_2 = -J_{s2} \quad (8.7)$$

Combining the above pairs of equations, we obtain

$$e_z \times (E_1 - E_2) = 0 \quad (8.8)$$

$$e_z \times (H_1 - H_2) = J_{s1} + J_{s2} = J_s \quad (8.9)$$

which apply to the fields on both sides of the patch. Eqns. 8.4–8.9 are written in terms of the total fields. However, since the excitation fields are assumed to be continuous, the boundary conditions (eqns. 8.4–8.5) and (eqns. 8.8–8.9) also hold for the diffracted fields. Hence the diffracted tangential electric field is continuous across the patch, while the jump in the diffracted tangential magnetic field equals the total surface current on the patch.

Finally, the boundary conditions on the ground plane  $z = -h$  are

$$e_z \times E_2 = 0 \quad (8.10)$$

$$e_z \times H_2 = J_s \quad (8.11)$$

It must be pointed out that the microstrip antenna problem can be completely solved without actually knowing the exact distribution of surface current on the ground plane. In fact, image theory can be used to remove the ground plane and the boundary conditions (eqns. 8.10–8.11) will then be included automatically in the Green's functions.

### 8.2.2 Potentials for the diffracted fields

Since no volume sources are considered in this model, the diffracted fields satisfy the homogeneous Maxwell's curl equations:

$$\nabla \times E^d = -j\omega\mu_0 H^d \quad (8.12)$$

$$\nabla \times H^d = j\omega\epsilon E^d \quad (8.13)$$

The resolution of antenna problems can in many cases be simplified by introducing the scalar and the vector potentials for the diffracted fields:

$$\mathbf{H}^d = (1/\mu_0) \nabla \times \mathbf{A} \quad (8.14)$$

$$\mathbf{E}^d = -j\omega \mathbf{A} - \nabla V \quad (8.15)$$

subject to Lorentz's gauge:

$$\nabla \cdot \mathbf{A} + j\omega \mu_0 \epsilon V = 0 \quad (8.16)$$

Introducing the above expressions into Maxwell's equations 8.12 and 8.13 and combining, we obtain two homogeneous Helmholtz's equations for the potentials:

$$(\nabla^2 + k_i^2) \mathbf{A} = 0 \quad (8.17)$$

$$(\nabla^2 + k_i^2) V = 0 \quad (8.18)$$

where  $k_i = \omega(\mu_0 \epsilon_i)^{1/2}$  is the wavenumber in medium  $i$ .

It must be recalled here that the choice of the couple  $\mathbf{A}$ ,  $V$  is not unique [2]. Indeed, any vector  $\mathbf{A}^* = \mathbf{A} + \text{grad } \Psi$  can be used as a new vector potential provided that the scalar potential is replaced by  $V^* = V - j\omega \Psi$ . Moreover, if  $\Psi$  is a solution of the homogeneous Helmholtz's equation, the new potential will still satisfy Lorentz's gauge (eqn. 8.16). We shall discuss later some convenient choices for the potentials.

### 8.2.3 Green's functions

Let us consider an arbitrarily oriented Hertz dipole of moment  $I d\mathbf{l}$  located at the point  $\mathbf{r}'$  (Fig. 8.3). In general, the vector potential at the point  $\mathbf{r}$  due to this dipole is given by the linear relationship

$$\mathbf{A}(\mathbf{r}) = \bar{\bar{\mathbf{G}}}_A(\mathbf{r}|\mathbf{r}') \cdot I d\mathbf{l} \quad (8.19)$$

where  $\bar{\bar{\mathbf{G}}}_A$  is a three-dimensional dyadic Green's function. The physical meaning of  $\bar{\bar{\mathbf{G}}}_A$  is evident: the scalar component  $G_A^s$  gives the  $s$ -component of the vector potential existing at the point  $\mathbf{r}$  created by a  $t$ -directed Hertz dipole located at the point  $\mathbf{r}'$ .

If the source and the observer are surrounded by an infinite homogeneous medium, the dyadic  $\bar{\bar{\mathbf{G}}}_A$  is diagonal and can be expressed as the product of a scalar Green's function  $G_A$  times the unit dyadic  $\bar{\mathbf{U}}$ . In this case, the vector potential is always colinear with the source dipole.

For a microstrip antenna it is possible to use a scalar free-space Green's function of the vector potential. However, if we do, we then need to use fictive electric and magnetic surface currents on the air-dielectric interface in order to satisfy the boundary conditions. These currents are also unknowns in the integral-equation formulation of the problem and add to the complexity of the numerical solution. The preferred solution is to include in the Green's functions

effects of the dielectric substrate and of the ground plane. Therefore, the Green's functions must satisfy the boundary conditions (eqns. 8.4–8.5) and (eqns. 8.10–8.11). Moreover, the boundary condition for the magnetic field (eqn. 8.9) is automatically built into the formulation of the Green's functions. These functions are dyadics, and unfortunately do not have a closed analytical expression. However, once they are formulated and numerically evaluated, the only unknown which remains is the true electric surface-current distribution on the conducting patch.

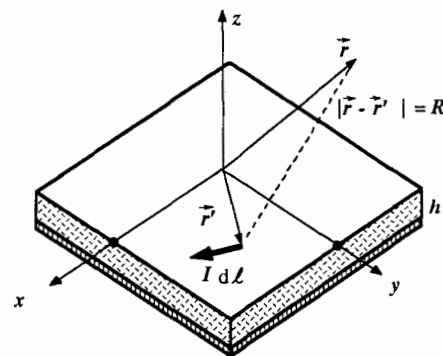


Fig. 8.3 Horizontal electric dipole (HED) on a microstrip substrate  
The fields and potentials of such an elementary source give the Green's functions associated with a microstrip antenna.

Keeping in mind the linearity of Maxwell's equations, the vector potential of a given current distribution can be written as a superposition integral involving the corresponding dyadic Green's function

$$\mathbf{A}(\mathbf{r}) = \int_{S_0} \bar{\bar{\mathbf{G}}}_A(\mathbf{r}|\mathbf{r}') \cdot \mathbf{J}_s(\mathbf{r}') dS' \quad (8.20)$$

The scalar potential  $V$  is obtained by introducing the above expression in the Lorentz gauge with the result:

$$j\omega \mu \epsilon V(\mathbf{r}) = - \int_{S_0} \nabla \cdot \bar{\bar{\mathbf{G}}}_A(\mathbf{r}|\mathbf{r}') \cdot \mathbf{J}_s(\mathbf{r}') dS' \quad (8.21)$$

The Green's function  $G_V$  associated with the scalar potential must be carefully defined. In fact, the uniqueness of  $G_V$  is guaranteed only if the divergence of  $\bar{\bar{\mathbf{G}}}_A$  is an irrotational vector. Thus we can write [3]

$$\nabla \cdot \bar{\bar{\mathbf{G}}}_A(\mathbf{r}|\mathbf{r}') = \mu \epsilon \nabla G_V(\mathbf{r}|\mathbf{r}') = -\mu \epsilon \nabla' G_V(\mathbf{r}|\mathbf{r}') \quad (8.22)$$

where  $\nabla'$  acts on the primed co-ordinates. Expression 8.21 is now easily transfor-

med into

$$V(r) = - \int_{S_0} G_V(r|r') \frac{\nabla' \cdot \mathbf{J}_s(r')}{j\omega} dS' + \int_{\partial S_0} G_V(r|r') \mathbf{J}_s(r') \cdot \mathbf{n} dS' \quad (8.23)$$

where  $\partial S_0$  is the perimeter of the patch and  $\mathbf{n}$  is the outwards-pointing normal unit vector (Fig. 8.2). The edge condition guarantees that the normal component of the surface current vanishes on the perimeter of the patch. Hence, the line integral in eqn. 8.23 can be eliminated.

We can now introduce the associated surface-charge density  $q_s$  via the continuity equation:

$$\nabla \cdot \mathbf{J}_s + j\omega q_s = 0 \quad (8.24)$$

Finally, we can express the scalar potential as:

$$V(r) = \int_{S_0} G_V(r|r') q_s(r') dS \quad (8.25)$$

It is worth mentioning that the edge condition can be applied even if  $S_0$  is a portion of a larger patch. Such a situation may arise when solving the problem with a method of moments using subsectional-basis functions. In this case the line integral in eqn. 8.23 can still be eliminated, but since  $\mathbf{J}_s$  does not necessarily vanish on the boundary of  $S_0$ , the continuity equation must be interpreted according to the theory of distributions, and delta functions corresponding to line charges in the boundary of  $S_0$ , will appear in the expression for  $q_s$ .

The Green's function  $G_V$  can be viewed as the scalar potential created by a point charge, even if isolated time-varying point charges do not exist in the real world. Thus, owing to the lack of a sound physical interpretation, it is better to consider  $G_V$  only as a useful mathematical device. Only when the frequency goes to zero, does this function become the familiar electrostatic potential of a point charge.

#### 8.2.4 Mixed potential integral equation (MPIE)

The diffracted fields derived from the potentials of eqns. 8.20 and 8.25 satisfy Maxwell's equations and the boundary conditions of the problem (eqns. 8.4–8.5) and (eqns. 8.8–8.9). The last step is now to relate these fields to the excitation fields via conditions (eqns. 8.6–8.7). If the total tangential electric field is forced to vanish on the patch surface, we get the standard electric field integral equation. This equation can be slightly modified to account for the ohmic losses on the patch. The total tangential electric field is now proportional to the total surface current, and we can write

$$\mathbf{e}_z \times (\mathbf{E}^e + \mathbf{E}^d) = \mathbf{e}_z \times \mathbf{Z}_s \mathbf{J}_s \quad (8.26a)$$

or, introducing the potentials

$$\mathbf{e}_z \times (j\omega \mathbf{A} + \nabla V + \mathbf{Z}_s \mathbf{J}_s) = \mathbf{e}_z \times \mathbf{E}^e \quad (8.26b)$$

where the proportionality constant  $\mathbf{Z}_s$  is a surface impedance (measured in

ohms) which accounts for the finite conductivity of the patch. An accurate value for  $\mathbf{Z}_s$  can only be obtained by measurement since  $\mathbf{Z}_s$  must include technological data such as the thickness and roughness of the metallic patch. However, in most cases the patch is thick compared with the skin depth  $\delta$ , and the classical expression

$$\mathbf{Z}_s = (1 + j)/\sigma^* \delta \quad (8.27)$$

represents a good approximation. In the above expression  $\sigma^*$  is an effective conductivity that includes roughness effects and can be several times lower than the values of conductivity found in standard tables.

Finally, introducing the integral form of the potentials (eqns. 8.20–8.21) in eqn. 8.26 we get the final expression for the mixed potential integral equation (MPIE):

$$\mathbf{e}_z \times (j\omega \int_{S_0} \bar{\mathbf{G}}_A \cdot \mathbf{J}_s dS' + \nabla \int_{S_0} G_V q_s dS' + \mathbf{Z}_s \mathbf{J}_s) = \mathbf{e}_z \times \mathbf{E}^e \quad (8.28)$$

The validity of this equation depends on the possibility of defining the Green's function  $G_V$  by eqn. 8.22.

Eqn. 8.28 is a Fredholm integral equation of the second kind. However, the term  $\mathbf{Z}_s \mathbf{J}_s$  is usually small and the iterative techniques commonly used for Fredholm integral equations of the second kind that arise, for example, when using the magnetic field integral equation [4], do not apply here.

The unknowns in the integral equation 8.28 are the surface current  $\mathbf{J}_s$  and the surface charge  $q_s$ . However, they are not independent, and are related through the continuity equation.

#### 8.2.5 Sketch of the proposed technique

The successive steps in solving the microstrip antenna problem are now clear. We start with the theoretical determination of the required Green's functions  $\mathbf{G}_A$  and  $G_V$ . In general, the Green's functions are available as definite integrals over semi-infinite intervals and they must be numerically evaluated for distances ranging from zero to the maximum linear dimension of the patch. The construction of accurate numerical integration algorithms to evaluate the Green's functions is a crucial step of the overall problem.

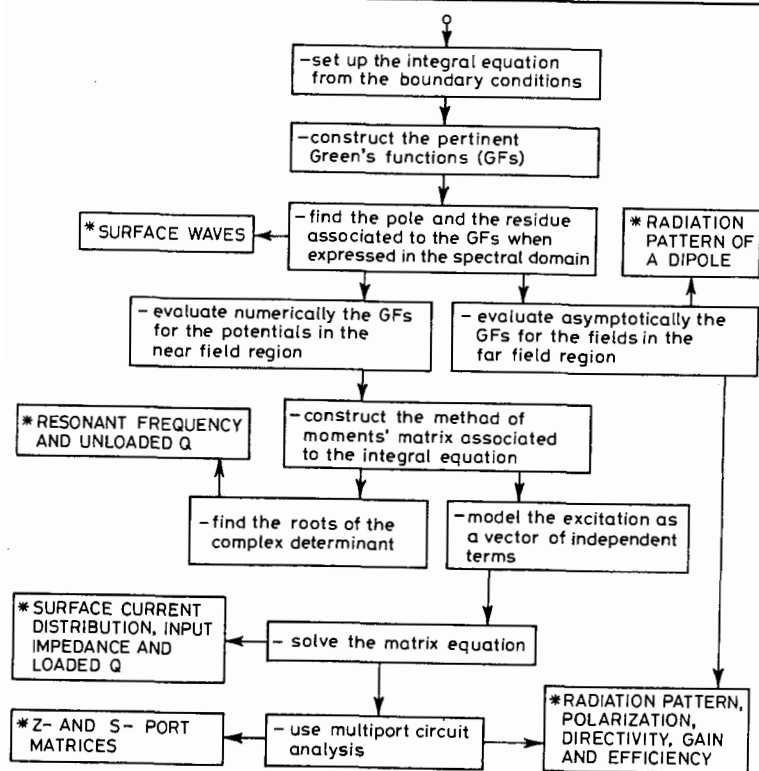
Once the Green's functions are computed, the unknown surface current is expanded over a set of basis functions and the integral equation is tested against a set of test functions using the so-called method of moments (MoM). Here, the correct choice of these sets of functions is essential for the quality of the final results. In this way, the integral equation is discretised and transformed into a set of linear equations. The complex eigenvalues of the matrix equation provide the unperturbed resonant frequencies of the patch and its unloaded quality factor.

The next step is the construction of the excitation fields. These fields depend strongly on the physical nature of the excitation. In many cases (coaxial pin, microstrip line) the computation of the excitation fields calls for the same or

related Green's functions that were calculated for the MoM matrix. Testing the excitation fields yields the independent vector of the matrix equation.

The solution of the matrix equation gives a numerical estimation of the unknown surface current. Computing the voltages at the excitation points allows the determination of the impedance and scattering matrices of the antenna. Standard circuit analysis may be used to account for any load or for multiple excitations. Resonant frequencies and loaded quality factors are easily derived from the input impedance.

**Table 8.1** Essential steps (–) and main results (\*) of the proposed numerical technique



To calculate the radiation pattern we need to go back to the Green's functions and obtain their asymptotic forms in the far field. This can be done analytically and the radiation pattern of the antenna, including polarisation and phase information, is obtained by using a superposition integral over the patch.

Finally, integration of the far fields over the upper half-space will give the directivity of the antenna and an estimation of its efficiency and gain.

These steps are summarised in Table 8.1.

### 8.3 Horizontal electric dipole (HED) in microstrip

The construction of the Green's functions requires the determination of the fields created by a horizontal electric dipole (Hertzian dipole) located on the air–dielectric interface of a microstrip structure (Fig. 8.3).

The first investigations of a HED embedded within a stratified medium are due to Sommerfeld, who published in 1909 the exact solution for a dipole over an imperfect ground. The Hankel integral transforms which appear within such a problem are often known as Sommerfeld integrals.

The vertical dipole over a conducting plane covered with a dielectric layer was studied by Lo and Brick in two articles which appeared almost simultaneously [5, 6]. The problem is quite similar to the one arising in microstrip antennas, except for the dipole orientation. However, even though the first microstrip lines were introduced around the time these articles were published, no connection between the two fields was made – microstrip antennas were to be developed some 20 years later. This may explain the different approaches to the two problems, in particular the absence of a detailed study of the near field, which is essential when the source and the observer are both located on the surface of the substrate.

The general theory of dipoles – either electric or magnetic, horizontal or vertical, located within an arbitrary stratified medium – was developed later, mainly by Brekhovskikh [7], Wait [8], Felsen and Marcuvitz [9], and Kong [10]. However, as was done in previous publications, the emphasis was put on the study of radiated fields, for which approximate asymptotic analysis is sufficient.

For the accurate study of microstrip radiation, however, precise knowledge of the surface currents on the patch, and hence of the near fields on the dielectric interface, are required. For this reason, the fields created by a HED located on the air – dielectric interface will be determined.

#### 8.3.1 The vector potential

Let us consider a HED of moment  $Idx$  equal to unity placed at the point  $r' = 0$  as indicated in Fig. 8.4.

In order to ease the mathematical development required for solving the Helmholtz equation 8.17 satisfied by the vector potential, we will replace the space variables  $x, y$  by their spectral counterparts  $k_x, k_y$  according to the double Fourier transform:

$$\tilde{f}(k_x, k_y) = \mathcal{F}[f(x, y)] = \frac{1}{2\pi} \int_{-\infty}^{\infty} \int_{-\infty}^{\infty} f(x, y) \exp(-jk_x x - jk_y y) dx dy \quad (8.29)$$

$$f(x, y) = \mathcal{F}^{-1}[\tilde{f}(k_x, k_y)] \\ = \frac{1}{2\pi} \iint_{-\infty}^{\infty} \tilde{f}(k_x, k_y) \exp(jk_x x + jk_y y) dk_x dk_y \quad (8.30)$$

In the spectral domain the homogeneous Helmholtz equation becomes:

$$\left(\frac{d^2}{dz^2} + u_i^2\right) \tilde{A} = 0$$

where

$$u_i^2 = k_x^2 + k_y^2 - k_i^2 = k_e^2 - k_i^2 \quad (8.31)$$

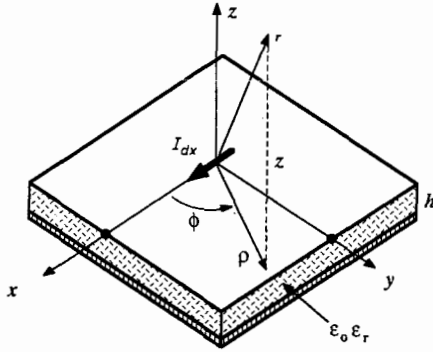


**Fig. 8.4** Co-ordinate system for the study of an  $x$ -directed horizontal electric dipole (HED) on a microstrip substrate  
The air-dielectric interface is at  $z = 0$  and the ground plane is at  $z = -h$ . The continuity equation implies that there are two point charges of value  $\pm I dx / j\omega$  at both extremities of the dipole

According to eqn. 8.1 we shall adopt from now on the shorthand notation  $u_1^2 = u_0^2 = k_e^2 - k_0^2$  and  $u_2^2 = u^2 = k_e^2 - \epsilon_r k_0^2$ .

The general solution of eqn. 8.31 for a cartesian component of  $A$  is ( $s = x, y, z$ ):

$$\tilde{A}_s = a \exp(-u_i z) + b \exp(+u_i z) \quad (8.32)$$

where the unknown factors  $a, b$  may be functions of the spectral variables.

The fields are obtained by using eqns. 8.14–8.15 and the Lorentz gauge, which also holds in the spectral domain. Since no external excitation fields are considered here, the fields of eqns. 8.14–8.15 are total fields. These fields must satisfy the boundary conditions eqns. 8.4–8.5 on the interface and eqn. 8.10 on the ground plane. In particular, the HED is equivalent to a surface current density in the plane  $z = 0$  given by:

$$\mathbf{J}_s = \mathbf{e}_x \delta(x) \delta(y) \Rightarrow \mathbf{J}_s = \mathbf{e}_z (1/2\pi) \quad (8.33)$$

If the dipole is embedded in an infinite homogeneous medium of permittivity  $\epsilon_0$ , the vector potential is parallel to the dipole and exhibits a spherical symmetry:

$$\mathbf{A} = \mathbf{e}_x \frac{\mu \exp(-jk_0 r)}{4\pi r} \Rightarrow \tilde{\mathbf{A}} = \mathbf{e}_x \frac{\mu}{4\pi} \exp(-u_0 |z|) / u_0 \quad (8.34)$$

On the other hand, it is well known [11] that two cartesian components of  $A$  are needed to satisfy the boundary conditions in an inhomogeneous structure such as a microstrip antenna. Here, we shall adopt Sommerfeld's choice and postulate an additional vertical component for the vector potential. Hence  $\mathbf{A} = \mathbf{e}_x A_x + \mathbf{e}_z A_z$ .

Choosing now for  $A_x$  and  $A_z$  general expressions of the form of eqn. 8.32, we obtain after satisfying the boundary conditions the expressions:

$$\tilde{A}_x = \frac{\mu_0}{2\pi} \left\{ \frac{\exp(-u_0 z) / D_{TE}}{\sinh u(z+h) / (D_{TE} \sinh uh)} \right\} \quad (8.35)$$

$$\tilde{A}_z = \frac{\mu_0}{2\pi} (\epsilon_r - 1) jk_x \left\{ \frac{\exp(-u_0 z) / (D_{TE} D_{TM})}{\frac{\cosh u(z+h)}{(D_{TE} D_{TM} \cosh uh)}} \right\} \quad (8.36)$$

where  $D_{TE} = u_0 + u \coth uh$ ,  $D_{TM} = \epsilon_r u_0 + u \tanh uh$ , and the upper and lower expression inside the symbol  $\{ \}$  correspond, respectively, to the upper semi-infinite medium ( $z > 0$ ) and to the substrate ( $-h < z < 0$ ).

It can be easily shown that if  $\epsilon_r = 1$  and  $h \rightarrow \infty$ , the vertical component  $A_z$  vanishes and  $A_x$  becomes the free-space vector potential given by eqn. 8.34.

### 8.3.2 Scalar potential and the fields

The continuity equation applied to an electric dipole implies the existence of two point charges  $q = \pm I / j\omega$  at both ends of the dipole.

Since the product  $I dx$  has been assumed to be equal to unity, the moment of this pair of charges is  $q dx = 1 / j\omega$ . The scalar potential associated with the dipole is given directly by the Lorentz gauge. Introducing eqns. 8.35 and 8.36 in eqn. 8.16 we get:

$$\tilde{V} = - \frac{jk_x}{2\pi j\omega \epsilon_0} \left\{ \frac{N \exp(-u_0 z) / (D_{TE} D_{TM})}{N \sinh u(z+h) / (D_{TE} D_{TM} \sinh uh)} \right\} \quad (8.37)$$

with  $N = u_0 + u \tanh uh$ .

In the space domain, the scalar potential  $V$  of an electrostatic dipole of moment  $1/j\omega$  is related to the scalar potential  $V_q$  of a single unit point charge by the well known expression:

$$V = - \frac{1}{j\omega} \frac{\partial V_q}{\partial x} \quad (8.38)$$

or, in the spectral domain by

$$\tilde{V} = -\frac{jk_x}{j\omega} \tilde{V}_q \quad (8.39)$$

Comparing eqn. 8.39 with eqn. 8.37, we can deduce by analogy that the potential of a unit point charge on the air-dielectric interface of a microstrip antenna is given by

$$\tilde{V}_q = \frac{1}{2\pi\epsilon_0} \left\{ \frac{N \exp(-u_0 z)/(D_{TE} D_{TM})}{\frac{N \sinh u(z+h)}{D_{TE} D_{TM} \sinh uh}} \right\} \quad (8.40)$$

Now, the construction of the fields is straightforward, for we have in the spectral domain:

$$\begin{aligned} \tilde{E}_x &= -j\omega \tilde{A}_x - jk_x \tilde{V} & \mu \tilde{H}_x &= jk_y \tilde{A}_z \\ \tilde{E}_y &= -jk_y \tilde{V} & \mu \tilde{H}_y &= (\partial \tilde{A}_x / \partial z) - jk_x \tilde{A}_z \\ \tilde{E}_z &= j\omega \tilde{A}_z - (\partial \tilde{V} / \partial z) & \mu \tilde{H}_z &= -jk_y \tilde{A}_x \end{aligned} \quad (8.41)$$

It can be easily demonstrated that the vertical component  $E_z$  shows the expected jump discontinuity when crossing the air-dielectric interface.

### 8.3.3 Surface waves and the spectral plane $k_\rho$

It can be shown [12] that the equations  $D_{TE} = 0$ ,  $D_{TM} = 0$  are the characteristic equations for the TE and TM surface-wave modes propagating on a dielectric-coated conducting plane. Hence the zeros of  $D_{TE}$  and  $D_{TM}$  give the phase constant of the surface waves existing on a microstrip structure.

The terms  $D_{TE}$  and  $D_{TM}$  depend on  $k_x$  and  $k_y$  only through the radial spectral variable  $k_\rho^2 = k_x^2 + k_y^2$ . For functions exhibiting such a kind of dependence, the inverse Fourier transform 8.30 can be written as

$$\mathcal{F}^{-1}[\tilde{f}(k_\rho)] = \int_0^\infty J_0(k_\rho \rho) k_\rho \tilde{f}(k_\rho) dk_\rho \quad (8.42a)$$

and

$$\mathcal{F}^{-1}[jk_x \tilde{f}(k_\rho)] = -\cos \phi \int_0^\infty J_1(k_\rho \rho) k_\rho^2 \tilde{f}(k_\rho) dk_\rho \quad (8.42b)$$

where  $\rho$ ,  $\phi$  are polar co-ordinates and  $J_0$  is the Bessel function of zeroth order and first kind. The replacement of the double Fourier transform by Hankel transforms is of great utility when performing the numerical evaluation of the fields and potentials. For instance, if the observation point is also on the interface ( $z = 0$ ) we have:

$$A_x = \frac{\mu_0}{2\pi} \int_0^\infty J_0(k_\rho \rho) \frac{k_\rho}{D_{TE}} dk_\rho \quad (8.43a)$$

$$A_z = -\frac{\mu_0}{2\pi} \cos \phi (\epsilon_r - 1) \int_0^\infty J_1(k_\rho \rho) \frac{k_\rho^2}{D_{TE} D_{TM}} dk_\rho \quad (8.43b)$$

$$V_q = \frac{1}{2\pi\epsilon_0} \int_0^\infty J_0(k_\rho \rho) \frac{k_\rho}{D_{TE}} dk_\rho \quad (8.44)$$

Hence, the surface waves appear as poles of the integrands in the complex plane  $k_\rho = \lambda + jv$ . It can be shown [13] that  $D_{TE}$  has no zeros if  $k_0 h(\epsilon_r' - 1)^{1/2} < \pi/2$  and  $D_{TM}$  has only one corresponding to the dominant zero-cutoff TM surface wave. This condition is equivalent to the restriction:

$$f[\text{GHz}] \leq 75/\{h[\text{mm}] \sqrt{(\epsilon_r' - 1)}\} \quad (8.45)$$

For the sake of simplicity we shall assume from now on that this inequality holds. Higher frequencies would add new poles, but the analysis made for the single-pole case remains qualitatively valid.

For substrates with moderate losses the pole  $\lambda_p + jv_p$  lies slightly below the real axis ( $v_p < 0$ ) and its real part is bounded by  $1 < \lambda_p/k_0 < \epsilon_r'^{1/2}$  (Fig. 8.5).

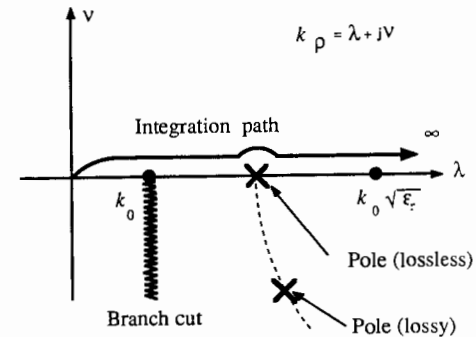


Fig. 8.5 Topology of the complex plane  $k_\rho$  with the original integration path from zero to infinity

The Figure also shows the geometrical locus of the pole as a function of dielectric losses.

More precisely, a good approximation for electrically thin substrates [14] is

$$\begin{aligned} \frac{\lambda_p}{k_0} &= 1 + (k_0 h)^2 \frac{(\epsilon_r' - 1)^2}{2\epsilon_r'^2} \\ v_p &= -(\epsilon_r' - 1) \tan \delta \left( \frac{k_0 h}{\epsilon_r'} \right)^2 \end{aligned} \quad (8.46)$$

The integration path of the Sommerfeld integral eqn. 8.43–8.44 is, in general, the real positive axis  $\lambda$ . But, if we consider the theoretical case of a lossless substrate, then  $v_p = 0$  and the pole is on the real axis. Since, by continuity, the integration path must remain above the pole, the integral from zero to infinity in the lossless



case is interpreted as:

$$\int_0^\infty = \oint_0^\infty - j\pi R \quad (8.47)$$

where the symbol  $\oint$  stands for Cauchy's principal value and  $R$  is the residue of the integral at the pole  $k_0 = \lambda_p$ .

Finally, it should be mentioned that the function  $u_0^2 = k_0^2 - k_0^2$  introduces a branch point at  $k_0 = k_0$  (Fig. 8.5). However, the integral remains bounded here and no deformation of the integration path is needed.

### 8.3.4 Far-field approximations

Far-field approximations are essential for the evaluation of the radiation pattern of a microstrip antenna. They can be obtained by using standard asymptotic techniques, such as the steepest-descent method [9]. We shall outline briefly the application of these techniques to Sommerfeld integrals. We begin by replacing the Bessel functions in these integrals by Hankel functions. This is done recalling the identity

$$\int_0^\infty J_0(k_0 \varrho) k_0 \tilde{f}(k_0) dk_0 = \frac{1}{2} \int_{-\infty}^\infty H_0^{(2)}(k_0 \varrho) k_0 \tilde{f}(k_0) dk_0 \quad (8.48)$$

which holds if  $\tilde{f}$  is an even function of  $k_0$  [11]. In this way, the integration path  $C$  in the complex plane  $k_0$  closes at infinity (Fig. 8.6) while the topology of the plane remains unchanged except for an additional branch point introduced by the Hankel function (Fig. 8.6). For the sake of clarity, the pole  $k_0 = \lambda_p$  is located on the real axis (lossless substrate, see Fig. 8.5).

Let us consider now a typical integral in the air:

$$I = \int_C H_n^{(2)}(k_0 \varrho) f(k_0) \exp(-u_0 z) dk_0 \quad (8.49)$$

where  $C$  is the path shown in Fig. 8.6.

To obtain an asymptotic expansion for  $I$ , the plane  $k_0$  is transformed into a new complex plane  $w$  defined by the relation

$$k_0 = k_0 \sin w \quad (8.50)$$

The transformed path  $C^*$  in the plane  $w$  is shown in Fig. 8.7. The pole is now located at  $w_p = \pi/2 + j \operatorname{arccosh}(\lambda_p/k_0)$  and the branch cuts associated with the points  $k_0 = \pm k_0$  disappear owing to the new choice of variables. Introducing spherical co-ordinates  $r, \theta$  ( $z = r \cos \theta, \varrho = r \sin \theta$ ) the argument of the Hankel function becomes

$$k_0 \varrho = k_0 r \sin \theta \sin w \quad (8.51)$$

Since we want an expression useful in the far field ( $k_0 r \gg 1$ ), we can replace the Hankel function by its first-order asymptotic expression. The integration path can be deformed far from the origin  $w = 0$  in order that  $\sin w$  never vanishes.

On the other hand, it can be shown [9] that this replacement will give correct results even for the broadside direction  $\theta = 0^\circ$ .

The final expression of the integral in the  $w$ -plane is

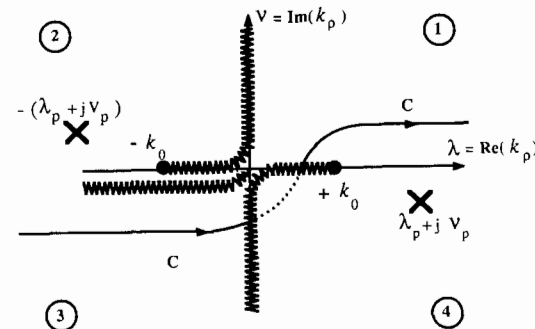


Fig. 8.6 The integration path  $C$  closing at infinity in the  $k_0$  plane and the new branch cut introduced by the Hankel function  
A portion (dotted line) of the path  $C$  is in the lower Riemann sheet

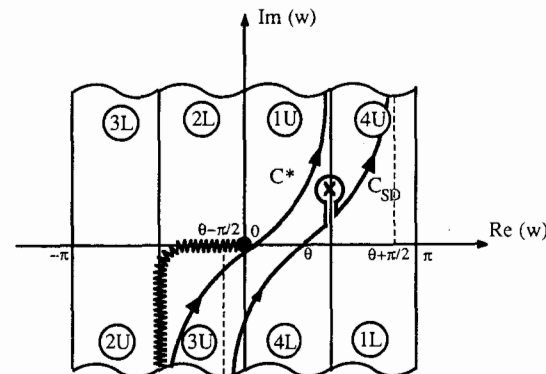


Fig. 8.7 The new complex plane  $w$  ( $k_0 = k_0 \sin w$ ) showing the transformed path  $C^*$ , the steepest descent path  $C_{SD}$  and the new location of the pole  
Also the correspondence with the four quadrants of the plane  $k_0$  is given, either in the upper (U) or in the lower (L) Riemann sheet.

$$I = \int_{C^*} F(w) \exp[\Omega q(w)] dw \quad (8.52)$$

$$F(w) = j^n \left( \frac{2j}{\pi \Omega \sin \theta \sin w} \right)^{1/2} k_0 \cos w f(k_0 \sin w)$$

with  $\Omega = k_0 r$  and  $q(w) = -j \cos(w - \theta)$ .

The saddle point  $w_s$  of function  $q$  is given by  $w_s = \theta$ . The steepest-descent path  $C_{SD}$  through  $w_s$  is defined by  $\text{Im}(q) = -1$ . Its particularities are easily derived (Fig. 8.7):

- (i)  $C_{SD}$  is at a  $45^\circ$  angle with the real axis.
- (ii)  $C_{SD}$  intersects the line  $\text{Re}(w) = \pi/2$  at the level  $\text{Im}(w) = \cosh^{-1}(1/\sin \theta)$ .
- (iii) As a result, the pole  $w_p$  is located between  $C_{SD}$  and the positive real axis only when  $\theta > \theta_p = \sin^{-1}(k_0/\lambda_p)$ .
- (iv)  $C_{SD}$  possesses two vertical asymptotes at  $\text{Re}(w) = \theta \pm \pi/2$ .

Contributions from the integrals joining the two paths  $C^*$  and  $C_{SD}$  at infinity can be eliminated since the term  $\exp(\Omega q)$  vanishes in these regions. The path  $C^*$  can then be deformed into the path  $C_{SD}$ , provided the contribution of the pole is added for angles greater than the critical angle  $\theta_p$ .

This is written symbolically as

$$\int_C = \int_{C_{SD}} + U(\theta - \theta_p) \int_{C_p} \quad (8.53)$$

where  $U$  is the Heaviside unit step function and  $C_p$  is a patch surrounding the pole  $w_p$  (Fig. 8.7).

The first-order approximation for the integral along  $C_{SD}$  can now be obtained by standard techniques [9]. The integral around the pole is evaluated using the residue theorem and is expressed in the original  $k_e$  plane.

Finally, the asymptotic expression of the integral  $I$  (eqn. 8.49), valid in the far field region, is

$$I \approx 2j^{n+1} \cotan \theta f(k_0 \sin \theta) \frac{\exp(-jk_0 r)}{r} [1 + 0(r^{-1})] - U(\theta - \theta_p) \times 2\pi j R H_n^{(2)}(\lambda_p \varrho) \exp[-z\sqrt{\lambda_p^2 - k_0^2}] [1 + 0(r^{-1})] \quad (8.54)$$

where the residue  $R$  is given by

$$R = \lim_{k_e \rightarrow \lambda_p} (k_e - \lambda_p) f(k_e) \quad (8.55)$$

and the Landau notation  $0(r^n)$  indicates the behavior at infinity of the first term neglected in the asymptotic expansion.

It must be noted here that the asymptotic approximation eqn. 8.54 is only valid if the pole  $\lambda_p$  is located far enough from the saddle point  $\lambda = k_0 \sin \theta$ , i.e.  $(k_0 \sin \theta - \lambda_p)r \gg 1$ . Otherwise, the contributions of the saddle point and of the pole cannot be separated and a modified saddle-point method must be used [9].

From the asymptotic point of view, the fields and potentials are the sum of two terms. The first term, due to the saddle point, represents a spatial wave with a complex factor depending on angle  $\theta$  and corresponds to the geometrical optical fields. The second term, due to the pole at  $\lambda_p$ , represents a cylindrical wave decreasing exponentially away from the substrate that corresponds to the surface wave.

The surface wave is only relevant for angles  $\theta > \theta_p$ , i.e. near the interface. However, its field dependence on  $q^{-1/2}$  can make it the dominant term of eqn. 8.54 when fields on the substrate surface at  $z = 0$  are evaluated.

**Radiated electric field:** An immediate application of the asymptotic relationship eqn. 8.54 is the computation of the radiated field. It is assumed here that  $\theta < \theta_p$ , so that the surface wave can be neglected. In a real situation, a substrate always has finite dimensions and the surface wave can be observed directly only close to the substrate. For angles near  $\theta = \pi/2$  (grazing angles) but far from the substrate, diffraction effects of the surface wave on the edges become significant.

The radiation field is obtained by transforming, for  $z > 0$ , the rectangular components of  $E$  (eqn. 8.41) into spherical components and then applying eqn. 8.54 to the resulting integrals. The final expressions are

$$\begin{aligned} E_\theta &= -j(Z_0/\lambda_0) \cos \phi g_\theta(\theta) \exp(-jk_0 r)/r \\ E_\phi &= j(Z_0/\lambda_0) \sin \phi g_\phi(\theta) \exp(-jk_0 r)/r \\ E_r &\sim 0 \end{aligned} \quad (8.56)$$

where  $Z_0$  is the free-space impedance,  $\lambda_0$  the free-space wavelength, not to be confused with the spectral variable  $\lambda = \text{Re}[k_e]$ , and

$$\begin{aligned} g_\theta(\theta) &= T \cos \theta / (T - j\epsilon_r \cos \theta \cotan k_0 h T) \\ g_\phi(\theta) &= \cos \theta / (\cos \theta - jT \cotan k_0 h T) \\ T &= (\epsilon_r - \sin^2 \theta)^{1/2} \end{aligned}$$

These asymptotic expansions have also been derived, with a different approach, by several other authors [15, 16]. The result for  $E_r$  shows that this component decreases faster with distance than  $1/r$ , and is thus not a radiated component.

Figs. 8.8 and 8.9 give the polar radiation patterns, respectively, in the  $E$ -plane and  $H$ -plane. In each Figure, four substrate thickness  $k_0 h = 0.05, 0.1, 0.2$  and  $0.5$  have been considered, and, for each thicknesses, curves corresponding to four dielectric constants  $\epsilon_r = 1, 2, 5$  and  $10$  have been plotted.

The presence of a dielectric layer increases, in general, the half-power beamwidth in the  $E$ -plane, especially for thin substrates. On the other hand, the  $H$ -plane pattern is almost independent of the substrate parameters, except for very thick substrates just on the threshold for the generation of a second surface wave.

**Potentials at the interface:** The Green's functions appearing in the integral equation 8.28 can be obtained from the potentials  $A_x$  and  $V_q$ . Solving the integral equation requires the knowledge of these potentials only at the interface. If we apply eqns. 8.54 to eqns. 8.43 and 8.44, transformed according to eqn. 8.48, we obtain with  $z = 0$  and  $\theta = \pi/2$ :

$$\frac{4\pi}{\mu} A_x \sim 0(q^{-2}) \quad (8.57)$$

$$4\pi\epsilon_0 V_q \sim -2\pi j R H_0^{(2)}(\lambda_p \varrho) \quad (8.58)$$

where the residue  $R$  is given by eqn. 8.55 with  $f = k_q N/D_{TE} D_{TM}$ . It is here apparent that the  $\varrho^{-1}$  contribution of the saddle point vanishes in both expressions. If higher-order terms in  $\varrho^{-2}$  are desired for  $A_x$ , which has no surface-wave component, the whole  $C_{SD}$  integration path in the complex plane  $k_q$  must be considered.

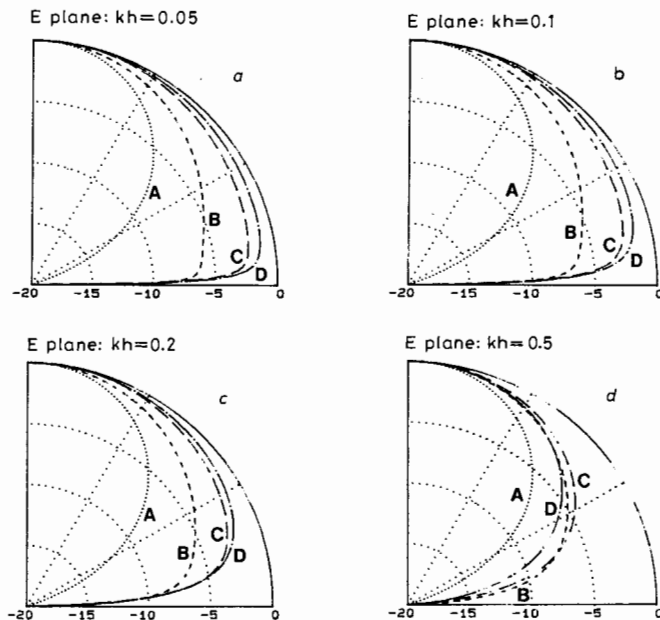


Fig. 8.8 Polar plot of the E-plane radiation pattern (in dB) of a HED on a microstrip substrate for four normalised substrate thicknesses  
(a)  $k_0 h = 0.05$  (b)  $k_0 h = 0.10$   
(c)  $k_0 h = 0.20$  (d)  $k_0 h = 0.50$   
A:  $\epsilon_r = 1$  B:  $\epsilon_r = 2$  C:  $\epsilon_r = 5$  D:  $\epsilon_r = 10$

It can be shown that the asymptotic behaviour of the integral is mainly determined by the discontinuity of the derivative of the integral at the point  $k_q = k_0$ . The dominant term in the asymptotic expansion is

$$\frac{4\pi}{\mu_0} A_x \approx \left( \frac{\tan \Delta}{\Delta} \right) \frac{2j \exp(-jk_0 \varrho)}{k_0 \varrho^2} \quad (8.59)$$

with the parameter  $\Delta$  defined as  $\Delta = k_0 h(\epsilon_r - 1)^{1/2}$ .

It is possible to replace eqn. 8.58 by a uniform asymptotic development valid

in all situations, but the calculations are rather complex, requiring error functions of complex arguments [9], and they will not be carried out here.

Asymptotic expressions 8.58 and 8.59 will be used in the following development to check the results obtained using numerical integration of the potentials.

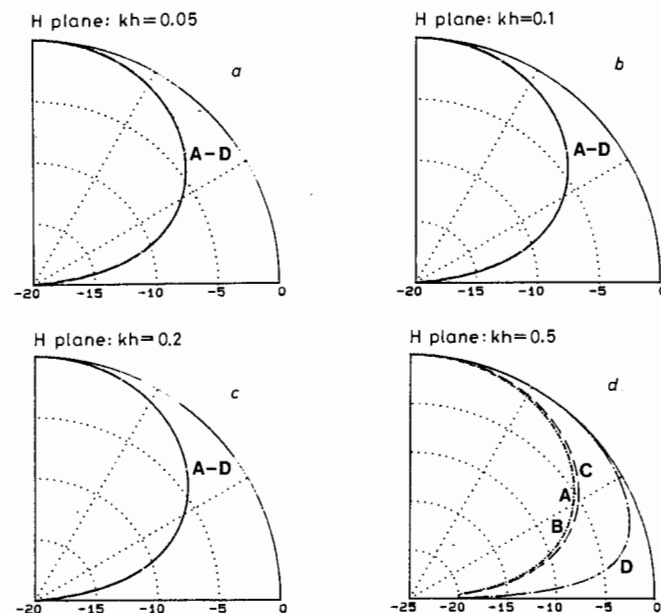


Fig. 8.9 Polar plot of the H-plane radiation pattern (in dB) of a HED on a microstrip substrate for four normalised substrate thicknesses  
(a)  $k_0 h = 0.05$  (b)  $k_0 h = 0.10$   
(c)  $k_0 h = 0.20$  (d)  $k_0 h = 0.50$   
A:  $\epsilon_r = 1$  B:  $\epsilon_r = 2$  C:  $\epsilon_r = 5$  D:  $\epsilon_r = 10$

### 8.3.5 Radiation resistance and antenna efficiency

If the cylindrical components of the fields are expressed in terms of the potentials by transforming eqns. 8.41, it can be shown that the term  $D_{TM}$  appears only in the denominator of components  $E_\phi E_z$  and  $H_\phi$ . Therefore, these are the components that include a surface-wave term, and thus the Poynting vector  $\mathbf{S}$  associated with the surface wave has a radial and a vertical component, respectively,  $S_\phi = -E_z H_\phi$  and  $S_z = E_\phi H_\phi$ . Consideration of the general expression 8.54 shows that the vertical component decreases exponentially with  $z$ , and consequently does not contribute to the radiated power. On the other hand, the

radial component can be written according to expression 8.54 as

$$S_\rho = (Z_0/2\pi k_0)(\epsilon_r - 1)\cos^2\phi R^2 (Idl)^2 \lambda_p^2 F(z)/\rho \quad (8.60)$$

with

$$F(z) = \begin{cases} \exp(-u_0 z)/D_{TE} \\ \cosh u(z+h)/D_{TE} \cosh uh \end{cases}$$

where the asymptotic expansion of the Hankel function has been used, and  $R$  is the residue of  $1/D_{TM}$  at the pole.

It can be shown that the integral of this component over a cylindrical surface of radius  $\rho$  extending from  $z = -h$  to infinity has a non-zero value independent of  $\rho$ . Hence, there is a net amount of power carried away by the surface wave. The surface integral must, in general, be numerically evaluated, essentially because there is no analytical formula for computing the pole  $\lambda_p$ . However, for thin substrates we can use the approximation given in eqn. 8.46 and estimate the residue appearing in eqn. 8.60 as:

$$R \approx \frac{\epsilon_r - 1}{\epsilon_r^2} k_0 h, \quad (8.61)$$

Then we define a radiation resistance  $R_{surf}$  associated with the surface wave as

$$R_{surf} \approx 8\pi^2 Z_0 \left(\frac{dl}{\lambda_0}\right)^2 \left(\frac{\epsilon_r - 1}{\epsilon_r} \frac{h}{\lambda_0}\right)^3 \quad (8.62)$$

In a similar fashion, we can introduce the radiation resistance  $R_{sp}$  associated with the space wave. Starting with the asymptotic expansions 8.56 for the fields and using the fact that in the far-field zone we have  $Z_0 \mathbf{H} = \mathbf{e}_r \times \mathbf{E}$  we can demonstrate that the Poynting vector is radial, its modulus being given by

$$S_r = Z_0 I^2 \left(\frac{dl}{\lambda_0}\right)^2 \frac{1}{r^2} (|g_\theta|^2 \cos^2\varphi + |g_\phi|^2 \sin^2\varphi) \quad (8.63)$$

Integrating this expression over the upper ( $z > 0$ ) half-sphere of radius  $r$  and equating the resulting power to  $I^2 R_{sp}$  we obtain the expression of the radiation resistance of the space wave:

$$R_{sp} = \pi Z_0 \left(\frac{dl}{\lambda_0}\right)^2 \int_0^{\pi/2} (|g_\theta|^2 + |g_\phi|^2) \sin\theta d\theta \quad (8.64)$$

As before, this surface integral cannot be analytically evaluated except for the case  $\epsilon_r = 1$  and  $h = \infty$ , where we recover the classical result for the radiation resistance of a Hertzian dipole radiating into free space.

However, for thin substrates we can again estimate the surface integral 8.64 by using the approximations:

$$g_\phi = \frac{jk_0 h(\epsilon_r - \sin^2\theta)}{\epsilon_r}; g_\theta = jk_0 h \cos\theta, \quad (8.65)$$

and we get

$$R_{sp} = 4\pi^3 Z_0 \left(\frac{dl}{\lambda_0}\right)^2 \left(\frac{h}{\lambda_0}\right)^2 \left(\frac{4}{3} - \frac{4}{3\epsilon_r} + \frac{8}{15\epsilon_r^2}\right) \quad (8.66)$$

Here again, the above formula becomes for  $\epsilon_r = 1$  the well known radiation resistance of a horizontal dipole above a ground plane [40]. It is worthwhile to compute numerically the integral 8.64 and plot the values of the radiation resistance  $R_{sp}$ , normalised to  $\pi Z_0 (dl/\lambda_0)^2$ , as a function of the parameter  $\Delta = k_0 h \sqrt{\epsilon_r - 1}$ , which is proportional to the substrate thickness and to the frequency. This has been done and the results are given in Fig. 8.10 for three values of the dielectric constant. Initially, the radiation resistance increases with the square of the thickness, as predicted by eqn. 8.66. But as the normalised thickness increases, the values of the resistance oscillate and show a discontinuous derivative at the points where  $\Delta$  is an odd multiple of  $\pi/2$ . These values correspond to the generation of higher-order surface waves [17].

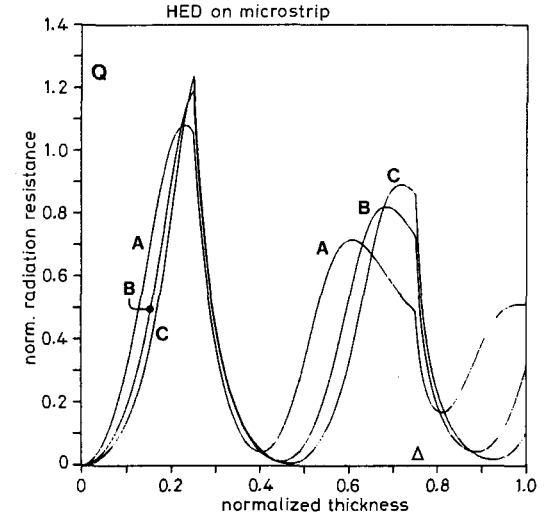


Fig. 8.10 Normalised radiation resistance  $Q = R_{sp}/[\pi Z_0 (dl/\lambda_0)^2]$  of a HED on a microstrip substrate as a function of the parameter  $\Delta = k_0 h \sqrt{\epsilon_r - 1}$ .  $Z_0 \approx 120\pi$  is the free-space wave impedance.

A:  $\epsilon_r = 2$

B:  $\epsilon_r = 3$

C:  $\epsilon_r = 4$

We can now evaluate the ratio between the power carried away by the surface wave and the power radiated by the space wave as:

$$q = \frac{\text{Power (surface wave)}}{\text{Power (spatial wave)}} = \pi^2 \frac{(\epsilon_r - 1)^3 h/\lambda_0}{\frac{2}{3} \epsilon_r^2 (\epsilon_r - 1) + \frac{4}{15} \epsilon_r} \quad (8.67)$$

which is proportional to the normalised thickness and shows a rather complicated dependence on the permittivity of the substrate. Finally, the radiation efficiency of a HED on a thin lossless microstrip substrate is given by

$$\eta = 1/(1 + q) \quad (8.68)$$

Numerical tests have shown eqn. 8.67 to be accurate for  $h \leq 0.05 \lambda_0$ . Fig. 8.11 gives the theoretical values of the efficiency for several dielectric constants.

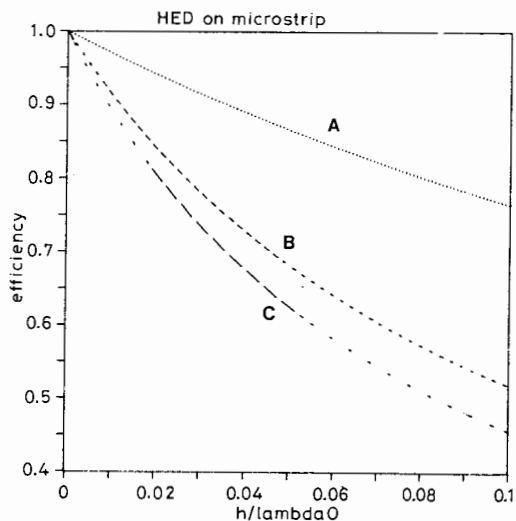


Fig. 8.11 Radiation efficiency (space-wave radiated-power/total radiated-power) of a HED on a lossless microstrip substrate as a function of the normalised substrate thickness  
A:  $\epsilon_r = 2$   
B:  $\epsilon_r = 5$   
C:  $\epsilon_r = 10$

**Finite size patches:** The above considerations refer to an elementary Hertzian dipole, but can be easily extended to finite-size microstrip patches by using superposition. The patch is excited by a unit current, and the input impedance  $Z_{IN}$  of the antenna is obtained with techniques to be described in the following Sections. Once the radiated fields are known, a radiation resistance  $R_{sp}$  is calculated using the techniques outlined in this Section. The overall antenna efficiency is given by the ratio  $R_{sp}/\text{Re}(Z_{IN})$ . If the antenna has been analysed assuming a lossless substrate and a perfect conductor, the conservation of power implies that  $R_{sp} + R_{surf} = \text{Re}(Z_{IN})$ . This is a useful check on the accuracy of the numerical calculations. Otherwise  $\text{Re}(Z_{IN})$  is greater than  $R_{sp} + R_{surf}$  and the difference gives the power dissipated in the antenna in the form of ohmic and dielectric losses.

The gain of the patch can now be defined in a customary way, as the product of the efficiency times the directivity.

#### 8.4 Numerical techniques for Sommerfeld Integrals

When a microstrip antenna is analysed by an integral-equation technique, it is necessary to evaluate the interaction between points separated by distances ranging from zero to several wavelengths. For most of these distances the accuracy of near- and far-field approximations is not sufficient and the potentials must be numerically evaluated. For a single-layer microstrip antenna the source and the observation point are both on the interface. Hence  $z = 0$  in the integral expressions for the fields and the potentials, and the exponential function which ensures convergence of the integrands disappears. This is the most difficult case numerically, and we will concentrate on it in this Section.

Even though many deformations of the original path  $C$  of Fig. 8.6 have been tried [14, 18], we feel that the integration along  $C$  (the real positive axis  $\lambda$  of the complex plane  $k_y$ ) provides the most efficient algorithm for evaluating the Sommerfeld integrals appearing in microstrip problems.

##### 8.4.1 Numerical integration on the real axis

The functions to be integrated oscillate on the real axis due to the Bessel functions. The square root  $u_0 = (\lambda^2 - k_0^2)^{1/2}$  introduces a discontinuity of the derivative at  $\lambda = k_0$  that corresponds to a branch point in the complex plane. If the integrand contains  $D_{TM}$  in the denominator there is a pole just below the real axis (or on the axis itself for a lossless substrate) that produces very strong variations of the integrands. Finally, many of the oscillating integrands have an envelope which converges very slowly ( $A_x$ ,  $V_q$ ) or even diverges at infinity ( $A_z$ ,  $V$ ). When the envelope diverges, the integral diverges in the Riemann sense since the area under the curve representing the integrand fails to converge to a finite value as the upper bound goes to infinity. However, the integral can be interpreted in the Abel sense as

$$\int_0^\infty F(\lambda) d\lambda = \lim_{z \rightarrow 0} \int_0^\infty F(\lambda) \exp(-u_0 z) d\lambda \quad (8.69)$$

and the exponential guarantees convergence. This means, physically, that the potentials at the interface can be considered as the limiting case of the potentials in the air when the height of the observation point above the interface goes to zero.

All these facts are clearly depicted in Fig. 8.12, which shows the integrand of the scalar potential  $V_q$  for  $\epsilon_{r1} = 2.55$ ,  $\tan \delta = 0$ ,  $k_0 h = 0.3\pi$ , and  $k_0 Q = 3$ . In this Figure, the substrate has been chosen quite thick for the sake of pictorial clarity. Electrically thinner, more common substrates will exhibit a pole very close to the branch point.

The integration interval is decomposed into three subintervals  $[0, k_0]$ ,  $[k_0, k_0\sqrt{\epsilon_r}]$  and  $[k_0\sqrt{\epsilon_r}, \infty]$ . In the region  $[0, k_0]$  the infinite derivative in  $k_0$  is eliminated with a change of variables  $\lambda = k_0 \cosh t$ . The resulting smoother function is integrated numerically. In the interval  $[k_0, k_0\sqrt{\epsilon_r}]$ , the singularity is first extracted if the integrand has  $D_{TM}$  in the denominator. By writing the function under the integral sign in the form  $F(\lambda) = J_n(\lambda\varrho)f(\lambda)$ , we have

$$F(\lambda) = [J_n(\lambda\varrho)f(\lambda) - F_{sing}(\lambda)] + F_{sing}(\lambda) \quad (8.70)$$

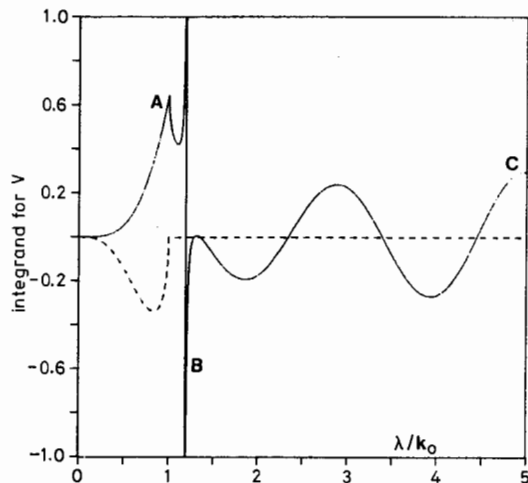


Fig. 8.12 Normalised values of the integrand associated with the scalar potential  $V$  of a HED on microstrip

$$\epsilon_r = 2.55 \quad k_0 h = 0.3\pi \quad k_0 \varrho = 3$$

A: Discontinuities in the derivative

B: Sharp peaks due to the pole

C: Oscillatory and divergent behaviour at infinity

— Real part    ---- Imaginary part

where

$$F_{sing}(\lambda) = \frac{R}{\lambda - (\lambda_p + j\nu_p)}$$

Here  $\lambda_p + j\nu_p$  is the complex pole ( $\nu_p \leq 0$ ) and  $R$  the residue of  $F$  at the pole. The function  $F_{sing}$  is integrated analytically as

$$\begin{aligned} I_{sing} &= \int_{k_0}^{k_0\sqrt{\epsilon_r}} F_{sing} d\lambda = \frac{R}{2} \ln \frac{(k_0\sqrt{\epsilon_r} - \lambda_p)^2 + \nu_p^2}{(\lambda_p - k_0)^2 + \nu_p^2} \\ &+ jR \arctan \frac{k_0\sqrt{\epsilon_r} - \lambda_p}{\nu_p} \\ &+ jR \arctan \frac{\lambda_p - k_0}{\nu_p} \end{aligned} \quad (8.71)$$

It is worth mentioning that, in the lossless case ( $\nu_p = 0$ ), the above integral becomes

$$I_{sing} = R \ln \frac{k_0\sqrt{\epsilon_r} - \lambda_p}{\lambda_p - k_0} - j\pi R = R \int_{k_0}^{k_0\sqrt{\epsilon_r}} \frac{d\lambda}{\lambda - \lambda_p} - j\pi R \quad (8.72)$$

and therefore the principal-value formulation (eqn. 8.47) of the lossless case is included as a limiting case in this numerical technique.

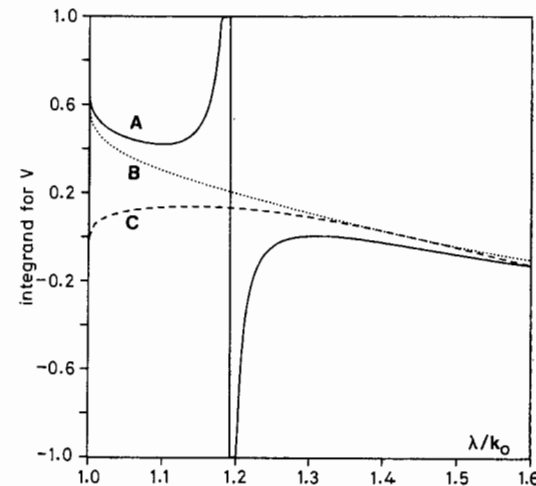


Fig. 8.13 Real part of the integrand of Fig. 8.12 for the lossy case in the interval  $[k_0, k_0\sqrt{\epsilon_r}]$

A: Before the extraction of the singularity

B: After the extraction of the singularity

C: After the change of variables:  $\lambda = k_0 \cosh t$

Fig. 8.13 depicts the real part of the original function  $F(\lambda)$  (solid line, A) and the difference  $F(\lambda) - F_{sing}(\lambda)$  (dotted line, B) after the singularity has been extracted. There is still an infinite derivative in the curve B at  $\lambda = k_0$ ; however, with a change of variables  $\lambda = k_0 \cosh(t)$  one finally obtains a very smooth integrand (the dashed line C in Fig. 8.13), which is integrated by a Gaussian quadrature. The same procedure is applied to the imaginary part of  $F(\lambda)$  to eliminate in a similar way the sharp peak and the infinite derivative.

Finally, in the region  $[k_0\sqrt{\epsilon_r}, \infty]$  we first extract the static term defined by  $F(\lambda, k_0 = 0)$ . Fig. 8.14 depicts the integrand  $F(\lambda, k_0)$  (curve A) and the difference  $F(\lambda, k_0) - F(\lambda, 0)$  (curve B). It can be shown that the static term has the form

$$F(\lambda, k_0 = 0) = C J_n(\lambda\varrho) \lambda^m \quad (8.73)$$

and hence it can be integrated analytically.

The remaining part is a slowly convergent oscillating function over a semi-infinite interval that is integrated with specially tailored techniques.

#### 8.4.2 Integrating oscillating functions over unbounded intervals

Sommerfeld integrals, as given by eqn. 8.42, can be grouped in a more general class of integrals defined by:

$$I(\varrho) = \int_a^\infty g(\lambda\varrho)f(\lambda) d\lambda \quad (8.74)$$

where

(a)  $g(\lambda\varrho)$  is a complex function whose real and imaginary parts oscillate with a strictly periodic behaviour (sin, cos), or behave asymptotically as the product of a periodic function and a monotonic function. A typical example of this class of functions, which will be termed from now on as quasi-periodic, are the Bessel functions of the first kind.

(b)  $f(\lambda)$  is a smooth, non-oscillating function which behaves asymptotically as  $\lambda^\alpha \exp(-\lambda z)$ . Therefore, for points on the interface ( $z = 0$ ), the function  $f(\lambda)$  decreases very slowly or even diverges at infinity if  $\alpha > 0$ . Here, we shall discuss the most interesting case,  $z = 0$ , which is also the most difficult from a numerical point of view. For the sake of simplicity,  $f(\lambda)$  is assumed to be real. Complex functions can be handled by working alternately with their real and imaginary parts.

(c) The lower integration bound  $a$  has been chosen conveniently to ensure that the interval  $[a, \infty)$  is far enough from any possible singularities of  $f(\lambda)$ . For instance in our problem, we shall take  $a = \sqrt{\epsilon_r}$ .

It is worth mentioning that the general expression 8.74 includes many integral transforms such as Fourier and Hankel transforms. Hence, the following techniques can be applied to many other problems in numerical analysis.

The classical problem involving Sommerfeld integrals is the problem of radio-wave propagation above a lossy ground, where the comprehensive monograph of Lytle and Lager is the classical reference [19]. These authors have found an iterative Romberg integration satisfactory, since here the integrand displays an exponential convergence and its poles have been removed from the real axis. In microstrip problems, Romberg integration has also been used, but its effectiveness decreases considerably in the absence of a well-behaved integrand.

In recent years, there has been a considerable amount of work published on the numerical evaluation of Fourier transforms, which are included in eqn. 8.74 as a particular case. The involved techniques can be classified in three groups.

(a) The decomposition  $[a, \infty] = [a, A] + [A, \infty]$ . Here, Filon's algorithm is applied to the finite interval  $[a, A]$ , while an asymptotic expression of the integrand is used to estimate the integral's value over  $[A, \infty]$  [20]. The most serious drawbacks of this approach are the choice of  $A$  and the analytical work

required – two features which are difficult to incorporate in an automatic computation routine.

(b) Another approach applies if  $g(\lambda\varrho)$  is a strictly periodic function. The following decomposition is then used:

$$\int_a^\infty g(\lambda\varrho)f(\lambda) d\lambda = \int_a^{a+P} g(\lambda\varrho) \sum_{n=0}^\infty f(\lambda + nP) d\lambda \quad (8.75)$$

where  $P$  is the period of the function  $g$ . The infinite sum under the integration sign can be evaluated using standard techniques such as Euler's transformation. Recently, a more involved technique using theoretical Fourier-transform concepts has been described in connection with a problem on quantum-mechanics impact cross-sections [21]. These methods work very well for large values of  $\varrho$  and an exponentially decreasing integrand. Unfortunately, their extension to quasi-periodic diverging integrands seems problematic.

(c) The third group of techniques, introduced by Hurwitz and Zweifel [22], are defined by the decomposition

$$\int_a^\infty g(\lambda\varrho)f(\lambda) d\lambda = \sum_{n=0}^\infty \int_{a+nP/2}^{a+(n+1)P/2} g(\lambda\varrho)f(\lambda) d\lambda \quad (8.76)$$

The integration over each half-cycle is performed prior to the series' summation. As before, an accelerating device, such as the nonlinear transformations of Shanks [23] and Sidi [24] can be used to sum the infinite series.

We feel that the decomposition 8.76 is particularly well suited for the Sommerfeld integrals encountered in microstrip problems and we have used it extensively throughout this work. However, instead of the sophisticated nonlinear techniques mentioned above, we have devised a new simple technique based on the concept of a weighted average between the half-cycle integrals [14]. This accelerating device has proved to be faster and more accurate for these kind of integrals.

### 8.5 Construction of the Green's functions

Once the potentials of a HED are known, the potentials created by an arbitrary surface current  $J_s$  existing on the plane  $z = 0$  can be determined by using the superposition integrals 8.20 and 8.25. The Green's functions arising in these expressions are closely related to the potentials of a HED and can be easily obtained if the symmetry properties of microstrip structures are taken into account.

We shall restrict ourselves here to the case where the source and observer are both on the air-dielectric interface ( $z = z' = 0$ ). Then, according to the translational invariance of the microstrip structure in any plane perpendicular

to the  $z$ -axis (eqn. 8.43), we have

$$\begin{cases} G_A^{xx}(\mathbf{r}|\mathbf{r}') = \frac{\mu_0}{2\pi} \int_0^\infty J_0(\lambda R) \frac{\lambda}{D_{TE}} d\lambda \\ G_A^{yy}(\mathbf{r}|\mathbf{r}') = 0 \\ G_A^{zz}(\mathbf{r}|\mathbf{r}') = -\frac{\mu_0}{2\pi} (\epsilon_r - 1) \cos \alpha \int_0^\infty J_1(\lambda R) \frac{\lambda^2}{D_{TE} D_{TM}} d\lambda \end{cases} \quad (8.77)$$

where the angle  $\alpha$  is given by  $\alpha = \tan^{-1}\{(y - y')/(x - x')\}$ . In short, we can say that the components  $G_A^{xx}$  and  $G_A^{zz}$  are given by the Sommerfeld integrals 8.43 with the polar co-ordinates  $\varrho$ ,  $\varphi$  replaced by  $R = |\mathbf{r} - \mathbf{r}'|$  and  $\alpha$ .

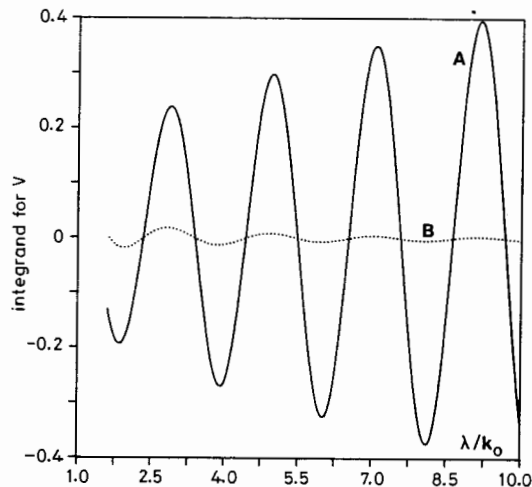


**Fig. 8.14** Real part of the integrand of Fig. 8.12 for the lossy case in the interval  $[k_0 \sqrt{\epsilon_r}, \infty)$   
A: Before the extraction of the static term  
B: After the extraction of the static term

In a similar way, since a microstrip substrate shows a symmetry of revolution around the  $z$ -axis, we can write

$$\begin{cases} G_A^{yy}(\mathbf{r}|\mathbf{r}') = G_A^{xx}(\mathbf{r}|\mathbf{r}') \\ G_A^{xy}(\mathbf{r}|\mathbf{r}') = 0 \\ G_A^{yz}(\mathbf{r}|\mathbf{r}') = -\frac{\mu_0}{2\pi} (\epsilon_r - 1) \sin \alpha \int_0^\infty J_1(\lambda R) \frac{\lambda^2}{D_{TE} D_{TM}} d\lambda \end{cases} \quad (8.78)$$

To evaluate  $G_A^{xz}$ ,  $G_A^{yz}$ ,  $G_A^{zz}$  we would need the potentials of a vertical electric

dipole. However, since only horizontal surface currents are considered we do not need to compute these expressions.

It is now a matter of straightforward algebra to show that the transverse divergence of the dyadic

$$\bar{\bar{G}}_A = \sum_{i=x,y,z} \sum_{j=x,y,z} e_i G_A^{ij} e_j \quad (8.79)$$

is given by

$$\nabla_i \cdot \bar{\bar{G}}_A = e_x \left( \frac{\partial G_A^{xx}}{\partial x} + \frac{\partial G_A^{zx}}{\partial z} \right) + e_y \left( \frac{\partial G_A^{yy}}{\partial y} + \frac{\partial G_A^{zy}}{\partial z} \right) \quad (8.80)$$

and, correspondingly, is derived from a scalar potential according to eqn. 8.22. Therefore, provided that no vertical currents are considered, it is possible to define a Green's function associated with the scalar potential as

$$G_r(\mathbf{r}|\mathbf{r}') = \text{eqn. 8.44 with } \varrho \text{ replaced by } |\mathbf{r} - \mathbf{r}'| = R. \quad (8.81)$$

This concludes the derivation of the Green's functions needed to solve the integral equation 8.28. A method-of-moments solution, described briefly in the next section, is used to numerically solve the equation and calculate the microstrip antenna parameters of interest.

## 8.6 Method of moments

The integral equation 8.28 will be numerically tackled with a method of moments (MoM). This technique [25] transforms the integral equation into a matrix algebraic equation which can be easily solved on a computer. The method of moments is among the most widespread numerical techniques in electromagnetics and a detailed account of the underlying principles will not be given here. For the problem of the microstrip antenna two particular versions of the MoM deserve attention: the subsectional-basis functions approach and Galerkin's method with entire domain-basis functions.

### 8.6.1 Rooftop (subsectional)-basis functions

If no a priori assumptions about the shape of the patches are made, a successful technique must decompose the patch into small elementary cells and define simple approximations for the surface current on each cell. The most commonly used shapes for the elementary cells are the triangle [26] and the rectangle. Even though the triangular shape is more flexible, rectangular cells involve simpler calculations and suffice for many microstrip antenna problems. Concerning the basis functions to be defined on these rectangular cells, a comparison of available possibilities [13] led to the selection of rooftop functions for the surface current  $\mathbf{J}_s$ , that have been successfully used in similar problems [27]. To implement these functions, the patch's boundary is replaced by a Manhattan-type



polygonal line (Fig. 8.15). As most commonly used antennas exhibit this kind of geometry anyway, this requirement is easily satisfied.

The patch's surface is then divided into rectangular cells, called charge cells, which, for the sake of clarity, will be assumed to be of identical size. This is not an essential requirement for the theory of the algorithm, but the use of different cell sizes considerably increases the computation time.

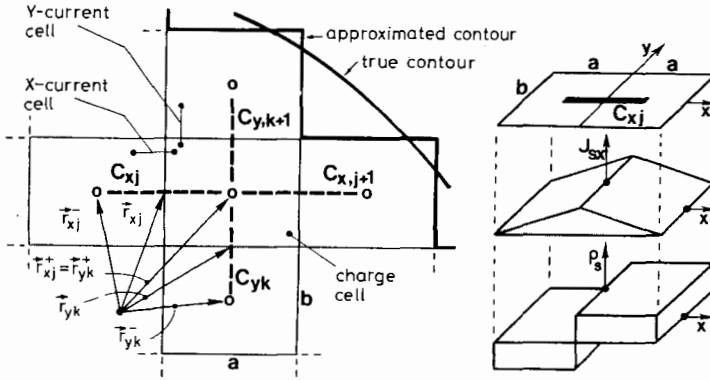


Fig. 8.15 Decomposition of the upper conductor in elementary cells showing the discretisation of the current and the test segments. After [38].

Two adjacent charge cells, sharing a common border perpendicular to the  $x$ -direction ( $y$ -direction) will form an  $x$ -directed ( $y$ -directed) current cell (Fig. 8.16). An automatic overlapping of current cells is obtained in this manner so that a particular charge cell may belong to up to four different current cells. The number of charge cells is thus related to the number of current cells, though the relationship is not a simple one, since it depends on the shape of the patch. However, for rectangular patches with  $m \times n$  charge cells, the number of  $x$ -directed current cells is  $M = (m - 1)n$ , and there are  $N = m(n - 1)$   $y$ -directed current cells.

Every current cell supports one rooftop basis function and there is one associated test segment joining the centres of the two charge cells making up the current cell. The centre of the segment  $C_{xj}$  associated with the  $j$ th  $x$ -directed current will be denoted by the vector  $\mathbf{r}_{xj}$ , and its ends by  $\mathbf{r}_{xj}^+$  and  $\mathbf{r}_{xj}^-$  (Fig. 8.16). These three vectors are related through

$$\mathbf{r}_{xj}^\pm = \mathbf{r}_{xj} \pm \mathbf{e}_x(a/2) \quad j = 1, 2, \dots, M \quad (8.82)$$

A similar relationship is written for  $y$ -directed segments  $C_{yj}$  ( $j = 1, 2, \dots, N$ ).

**Basis functions:** The Cartesian components of the surface current are expanded over a set of basis functions  $T_x, T_y$ :

$$\begin{aligned} J_{xx} &= \frac{1}{b} \sum_{j=1}^M I_{xj} T_x(\mathbf{r} - \mathbf{r}_{xj}) \\ J_{xy} &= \frac{1}{a} \sum_{j=1}^N I_{yj} T_y(\mathbf{r} - \mathbf{r}_{yj}) \end{aligned} \quad (8.83)$$

where the basis functions are rooftop-type functions shown in Fig. 8.16:

$$T_x(\mathbf{r}) = \begin{cases} 1 - |x|/a & |x| < a, |y| < b/2 \\ 0 & \text{elsewhere} \end{cases} \quad (8.84)$$

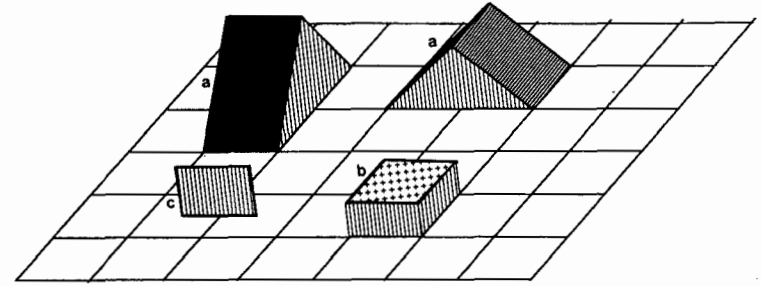


Fig. 8.16 Subsectional basis functions defined over pairs of adjacent cells (a), associated constant charge distribution on each cell (b), and razor testing functions (c)

A similar expression is obtained for  $T_y$  by interchanging  $a \leftrightarrow b$  and  $x \leftrightarrow y$  in the above equation.

The introduction of factors  $1/a$  and  $1/b$  in eqn. 8.83 yields unknown coefficients  $I_{xj}$  and  $I_{yj}$  having the dimensions of a current. Moreover, every coefficient gives the total current flowing across the common boundary of two charge cells.

The associated surface charge density is obtained from eqn. 8.83 by using the continuity equation, yielding

$$\begin{aligned} q_s &= \frac{1}{j\omega ab} \left\{ \sum_{j=1}^M I_{xj} [\Pi(\mathbf{r} - \mathbf{r}_{xj}^+) - \Pi(\mathbf{r} - \mathbf{r}_{xj}^-)] \right. \\ &\quad \left. + \sum_{j=1}^N I_{yj} [\Pi(\mathbf{r} - \mathbf{r}_{yj}^+) - \Pi(\mathbf{r} - \mathbf{r}_{yj}^-)] \right\} \end{aligned} \quad (8.85)$$

where  $\Pi(\mathbf{r})$  is a two-dimensional unit pulse function defined over a rectangle of dimensions  $a \times b$ , centered at  $\mathbf{r} = 0$ .

The charge density within every elementary cell remains constant, justifying the name charge cell. For the charge cell of Fig. 8.15, with four test segments ending at its centre, the surface charge density is simply given by

$$q_s = \frac{1}{j\omega ab} [I_{x,j+1} - I_{x,j} + I_{y,k+1} - I_{y,k}] \quad (8.86)$$

The charge density is discontinuous on the borders between charge cells. However, the scalar potential remains bounded, while the electric field becomes singular, since  $q_s$  does not satisfy a Hölder condition [13]. This means that the test functions must be selected carefully, avoiding the locations where the electric field is singular.

**Discrete Green's functions:** The notation and the computational task can be simplified by introducing 'discrete Green's functions', that have as a source a complete basis function, rather than the traditional elementary point source.

The vector potential  $\Gamma_A$  is created by a rooftop distribution of surface current, whereas  $\Gamma_V$  is the scalar potential resulting from a rectangular distribution of unit surface charge. In practice it is convenient to deal with dimensionless quantities and in a normalised space where physical lengths are replaced by electrical lengths. The following dimensionless expressions are therefore introduced that define the discrete Green's functions:

$$\Gamma_A^{xx}(\mathbf{r}|\mathbf{r}_{sj}) = \int_{S_{sj}} \frac{1}{\mu_0 k_0} G_A^{xx}(\mathbf{r}|\mathbf{r}') T_x(\mathbf{r}' - \mathbf{r}_{sj})(k_0^2 dS') \quad (8.87)$$

$$\Gamma_V(\mathbf{r}|\mathbf{r}_{0j}) = \int_{S_{0j}} \frac{\epsilon_0}{k_0} G_V(\mathbf{r}|\mathbf{r}') \Pi(\mathbf{r}' - \mathbf{r}_{0j})(k_0^2 dS') \quad (8.88)$$

A similar expression may be written for  $\Gamma_A^{yy}$ . In these formulas  $\mathbf{r}_{sj}(\mathbf{r}_{0j})$  denotes the centre of a test segment and  $S_{sj}(S_{0j})$  the surface of a current (charge) cell.

The discrete Green's functions exhibit the same properties of translational invariance and symmetry as the conventional Green's functions. In general, the surface integrals in eqns. 8.87 and 8.88 must be evaluated numerically. When the observation point  $\mathbf{r}$  belongs to the source cell, some difficulties arise in the integration process. It is then recommended that the singular part of the Green's function which corresponds to the dominant term of their static value be extracted, i.e.  $G = G_s + (G - G_s)$  where the static value  $G_s$  is given by:

$$G_A^{xx}(\mathbf{r}|\mathbf{r}') = \frac{\mu_0}{4\pi|\mathbf{r} - \mathbf{r}'|} \quad (8.89)$$

for the vector potential and

$$G_V(\mathbf{r}|\mathbf{r}') = \frac{1}{4\pi\epsilon_0|\mathbf{r} - \mathbf{r}'|} \quad (8.90)$$

for the scalar potential.

The singular part  $G_s$  can be analytically integrated over the cell's surface. For instance, the singular part of eqn. 8.88 is

$$2\pi(\epsilon_r + 1)\Gamma_V(0|0) \simeq 2k_0 a \ln \tan\left(\frac{\alpha}{2} + \frac{\pi}{4}\right) - 2k_0 b \ln \tan(\alpha/2) \quad (8.91)$$

with  $\tan \alpha = b/a$ .

When the observer is located many cells away from the sources, the sources can be concentrated at the centre of the cell. The following approximations may then be used:

$$\Gamma_A^{xx}(\mathbf{r}|\mathbf{r}_{xi}) \simeq \frac{1}{\mu_0 k_0} G_A^{xx}(\mathbf{r}|\mathbf{r}_{xi})(k_0 a)(k_0 b) \quad (8.92)$$

$$\Gamma_V(\mathbf{r}|\mathbf{r}_{0i}) \simeq \frac{\epsilon_0}{k_0} G_V(\mathbf{r}|\mathbf{r}_{0i})(k_0 a)(k_0 b)$$

**Test functions:** The last step of the solution with the moment method is the selection of a suitable test function. Previous work [13] has shown that the best choice, compatible with the basis functions selected, is the use of unidimensional rectangular pulses. The use of these test functions, also called razor test functions (see Fig. 8.16), is equivalent to integrating the boundary condition (eqn. 8.26) along the segments linking the centres of adjacent cells (test segments), and therefore the testing procedure yields equations of the type:

$$j\omega \int_{C_{xi}} A_x dx + V(\mathbf{r}_{xi}^+) - V(\mathbf{r}_{xi}^-) + Z_s \int_{C_{xi}} J_{sx} dx = \int_{C_{xi}} E_x^{(e)} dx = V_{xi}^{(e)} \quad (8.93)$$

where  $C_{xi}$  is the  $x$ -directed test segment extending from  $\mathbf{r}_{xi}^-$  to  $\mathbf{r}_{xi}^+$  and  $V_{xi}^{(e)}$  is the excitation (impressed) voltage along the segment. A similar relationship is obtained for  $y$ -directed test segments. It is worth mentioning that this choice eliminates the need for computing field values near the edges where field singularities can adversely affect the performance of the moment method.

Eqn. 8.93 is well suited for numerical treatment since all derivatives have been removed. The integration of  $J_{sx}$  can be done easily using the expansion given by eqn. 8.83 with the result

$$\int_{C_{xi}} J_{sx} dx = \frac{a}{4b} [2I_{xi} + I_{xi+1} + I_{xi-1}] \simeq \frac{a}{b} I_{xi} \quad (8.94)$$

The last approximation is valid for a reasonably smooth current distribution.

**The matrix equation:** Introducing the expansions 8.83 and 8.85 in eqn. 8.93 and using the discrete Green's functions defined above, the following matrix equation is obtained:

$$\begin{pmatrix} C^{xx} & C^{xy} \\ C^{yx} & C^{yy} \end{pmatrix} \begin{pmatrix} I_x \\ I_y \end{pmatrix} = \frac{1}{jZ_0} \begin{pmatrix} V_x^{(e)} \\ V_y^{(e)} \end{pmatrix} \quad (8.95)$$

The elements in the submatrices are given by

$$C_{ij}^{xx} = \frac{1}{k_0 a k_0 b} [-\Gamma_V(r_{xi}^+ | r_{xj}^-) - \Gamma_V(r_{xi}^- | r_{xj}^+) + \Gamma_V(r_{xi}^+ | r_{xj}^+) + \Gamma_V(r_{xi}^- | r_{xj}^-)] - \frac{1}{k_0 b} \int_{C_{xi}} \Gamma_A^{xx}(r | r_{xj}) k_0 dx + j \frac{Z_s a}{Z_0 b} \delta_{ij}$$

$$i = 1 \dots M, j = 1 \dots M \quad (8.96)$$

$$C_{ij}^{yy} = \frac{1}{k_0 a k_0 b} [-\Gamma_V(r_{yi}^+ | r_{yj}^-) - \Gamma_V(r_{yi}^- | r_{yj}^+) + \Gamma_V(r_{yi}^+ | r_{yj}^+) + \Gamma_V(r_{yi}^- | r_{yj}^-)]$$

$$i = 1 \dots M, j = 1 \dots N \quad (8.97)$$

where  $\delta_{ij}$  is the Kronecker delta. The expression for  $C_{ij}^{yy}$  is obtained by interchanging the couples  $(x, y)$ ,  $(a, b)$  and  $(M, N)$  within eqn. 8.96. Finally, it is easily shown that  $C_{ij}^{yx} = C_{ji}^{xy}$ .

For distances  $|r_{xi} - r_{xj}|$  much greater than the dimensions of a cell, the integrals in eqn. (8.96) can be replaced by

$$\int_{C_{xi}} \Gamma_A^{xx}(r | r_{xj}) k_0 dx \simeq k_0 a \Gamma_A^{xx}(r_{xi} | r_{xj}) \quad (8.98)$$

In principle, this approximation is not valid for short distances between cells. For these situations, however, the contribution of the vector potential is overshadowed by that of the scalar potential, so that the approximation of eqn. 8.98 still suffices. As a matter of fact, eqn. 8.98 may be used everywhere but on the diagonal terms. This approximation has been confirmed by extensive numerical tests.

A last point worth mentioning concerns the number of discrete Green's functions that must be calculated. For a rectangular patch with  $m \times n$  charge cells, the number of matrix elements is  $(M + N)^2$ , with  $M = (m - 1)n$  and  $N = (n - 1)m$ . When all the cells have identical sizes, only  $m \times n$  values of  $\Gamma_V$ ,  $M$  values of  $\Gamma_A^{xx}$  and  $N$  values of  $\Gamma_A^{yy}$  are needed in order to completely fill the matrix. This is the great advantage of using cells of equal size, and it is generally more convenient to use a larger number of identical cells rather than fewer cells of different sizes.

*Interpolation among Green's functions:* The evaluation of the matrix in eqn. 8.95 requires a large amount of computation. For a rectangular patch divided into  $10 \times 10$  cells, the order of the matrix is 180; hence the number of elements in the matrix is  $180^2 = 32400$ . Even when a simple  $4 \times 4$  Gaussian quadrature is used to evaluate the discrete Green's functions, the number of Sommerfeld integrals that need to be evaluated would exceed half a million.

Fortunately, for a given structure these integrals depend only upon the distance from source to observer. It is thus possible to tabulate the integrals for a small number of distances, and then to interpolate between the tabulated values. The distances to be considered range from zero to the maximum linear dimension of the patch. Several interpolation schemes have been tried [13]. The best solution was obtained by separating the Green's functions according to eqn. 8.89, and then using a simple parabolic Lagrange interpolation for the regular part.

For a square patch with  $10 \times 10$  cells, at frequencies for which the patch's length is less than a free-space wavelength, the error obtained when interpolating from 25 tabulated values is hardly noticeable: less than 0.5%, even though the computation time was reduced by a factor of 100!

### 8.6.2 Entire domain basis functions

If the microstrip patch has a simple regular shape (circular or rectangular) we can consider the equivalent electromagnetic cavity obtained when the patch is enclosed by a lateral magnetic wall. If the eigen modes have a simple analytical expression it is reasonable to use them as a set of entire domain basis functions. For thin substrates, the surface-current distribution on a microstrip patch at resonance follows closely the behaviour of the corresponding eigenmode except for a slight disturbance due to the antenna's excitation. Therefore, meaningful results can frequently be obtained by using a very small number of entire domain basis functions. This fact enables the analysis of microstrip arrays having hundreds of elements. The size of the linear system to be solved will be equal to two or three times the number of patches.

It is clear that if only one basis function is allowed per patch, we cannot use a poor testing procedure such as point matching and match the boundary condition only at the centre of the patch. The best alternative is provided by Galerkin's method where the test functions are identical to the basis functions and the inner product includes a surface integration over the patches [25].

To be clear, let us consider a single rectangular patch of dimensions  $L, W$ . The eigen modes of the corresponding cavity are [28]

$$f_j = e_x \sin \frac{m\pi x}{L} \cos \frac{n\pi y}{W} + e_y \cos \frac{m\pi x}{L} \sin \frac{n\pi y}{W} \quad (8.99)$$

where the co-ordinate origin is in the lower left corner of the patch. The vectors  $f_j$  correspond to the modes  $TM_{mn0}$  of the equivalent cavity. The choice of the modes  $TM_{mn0}$  in the expansion of  $J_s$  is rather arbitrary and depends on the problem considered. For instance, they can be ordered according to their resonant frequencies, or we can consider only the  $TM_{mn0}$  subset if variations along the co-ordinate  $y$  can be neglected. In any case, the relation between the integers  $m, n$  and the ordinal number  $j$  in eqn. 8.99 should be clearly defined.

We assume now for the unknown surface current density the following

expansion:

$$\mathbf{J}_s = \sum_j \alpha_j \mathbf{f}_j \quad (8.100)$$

and consequently

$$q_s = \sum_j \alpha_j \left( \frac{-\nabla \cdot \mathbf{f}_j}{j\omega} \right) = \sum_j \alpha_j h_j \quad (8.101)$$

Notice that here the unknown coefficients  $\alpha_j$  are interpreted as being amplitudes of the surface current distribution [A/m] while, when using subsectional basis, the unknowns were the total currents [A] flowing across contiguous cells.

If we test now the boundary condition 8.26 in the Galerkin sense, we get the set of equations

$$j\omega \int_{s_0} \mathbf{f}_i \cdot \mathbf{A} ds + \int_{s_0} \mathbf{f}_i \cdot \nabla V ds + Z_s \int_{s_0} \mathbf{f}_i \cdot \mathbf{J}_s ds = \int_{s_0} \mathbf{f}_i \cdot \mathbf{E}^{(e)} ds \quad (8.102)$$

The integral involving the scalar potential can be rewritten as

$$\int_{s_0} \mathbf{f}_i \cdot \nabla V ds = \frac{1}{j\omega} \int_{s_0} h_i V ds \quad (8.103)$$

where the identity  $\nabla \cdot (\mathbf{f}_i V) = \mathbf{f}_i \cdot \nabla V + V \nabla \cdot \mathbf{f}_i$  has been used.

Finally, introducing expansions 8.100 and 8.101 into eqn. 8.102 we get the linear system

$$\sum_j c_{ij} \alpha_j = b_i \quad \text{or} \quad \mathbf{C}\boldsymbol{\alpha} = \mathbf{b} \quad (8.104)$$

where

$$c_{ij} = j\omega \int_{s_0} \mathbf{f}_i \cdot \int_{s_0} \bar{\mathbf{G}}_A \cdot \mathbf{f}_j ds ds' + \frac{1}{j\omega} \int_{s_0} h_i \int_{s_0} G_v h_j ds ds' + Z_s \int_{s_0} \mathbf{f}_i \cdot \mathbf{f}_j ds \quad (8.105)$$

and

$$b_i = \int_{s_0} \mathbf{f}_i \cdot \mathbf{E}^{(e)} ds \quad (8.106)$$

The last term in the expression of  $c_{ij}$  vanishes if  $i \neq j$  due to the orthogonality of the eigenmodes  $\mathbf{f}_i$ .

It can be seen that, essentially, each matrix element requires the computation of two fourfold integrals. Fortunately, two of the four integrations can be performed analytically, by introducing the new variables  $u = x - x'$ ,  $u' = x + x'$ ,  $v = y - y'$ ,  $v' = y + y'$ . As in the subsectional basis case, the elements  $c_{ij}$  will include a singularity when  $\mathbf{r} = \mathbf{r}'$  in the Green's functions. Again, a decomposition of the type of eqn. 8.89 or a change to polar co-ordinates may be used to eliminate the singularity.

The above techniques can easily be generalised to the analysis of an array of patches. In this case, the domains of the  $i$ th and  $j$ th modes do not necessarily coincide. If the distance between the centres of the patches is greater than the largest linear dimension of a single patch, we can use the approximation

$$\int_{s_0} g_i \int_{s_j} G(\mathbf{r}|\mathbf{r}') g_j ds ds' \simeq G(\mathbf{r}_i|\mathbf{r}_j) \int_{s_i} g_i ds \int_{s_j} g_j ds' \quad (8.107)$$

where  $\mathbf{r}_i, \mathbf{r}_j$  denote the centres of the patches.

More accurate approximations can be obtained by expanding the Green's functions in a Taylor series. These mathematical tools and powerful numerical integration routines enable the total computation time to be kept within reasonable limits.

## 8.7 Excitation and loading

In practice, microstrip antennas are excited by many different techniques. A good survey of these has been recently given by Pozar [29]. This Section will present a brief description of those most commonly found, keeping in mind that the method of moments will be used to analyse the antenna.

### 8.7.1 Several microstrip-antenna excitations

A very common technique used for feeding a microstrip antenna consists of a microstrip line directly connected to the patch. A thorough treatment of this excitation requires the analysis of the incident and reflected quasi-TEM current waves existing on the line, which is assumed to extend from the patch to infinity. A more realistic model assumes that the microstrip line has a finite length and introduces a mathematical excitation (for instance, a filament of vertical current or a series voltage generator) at the end of the line. The vertical filament of current is a good model for the coaxial excitation and on a physical basis is preferred to the series voltage generator. The microstrip line is then cut at a point where uniform line conditions can be assumed. In this way the discontinuity created by the line-patch junction, and possibly discontinuities of the line itself, are included in the analysis. If a vertical filament of unit current is used as excitation, the input impedance is simply the voltage at the insertion point. When using other mathematical excitations, the section of line included in the analysis must be long enough to support a standing-wave pattern that can be used to estimate the input impedance of the patch.

Finally, it is worth mentioning that replacing the microstrip line by a coaxial probe at the edge of the patch is a first-order approximation that gives surprisingly good results in many practical cases.

*Microstrip line under the patch:* A more sophisticated excitation, designed to minimise the spurious radiation coming from the feed line, uses a microstrip line under the patch to couple energy to it electromagnetically [29, 30]. The presence

of two dielectric layers adds an additional degree of freedom to the design. The comments made above for the line directly connected to the patch also apply here. The microstrip line can be cut far from the patch and terminated in a coaxial probe or excited by some other mathematical device.

**Slot in the ground plane:** A slot in the ground plane can be used to couple energy to the patch from, presumably, a triplate transmission line [31]. The mathematical treatment replaces the slot by an equivalent distribution of surface magnetic current. The excitation field  $E^{(e)}$  results from this current. In the numerical procedure, this modifies only the independent terms  $b_i$  (eqn. 8.106).

### 8.7.2 Coaxial excitation and input impedance

A coaxial line attached to the bottom of the patch (Fig. 8.17) is also a practical way of feeding microstrip patches. From a theoretical point of view, the coaxial excitation is of great interest because simple yet accurate mathematical models are available. While the models presented here are constant current or voltage sources and not constant power sources, that are actually used in practice, the calculated values of the input impedance agrees closely with measured results.

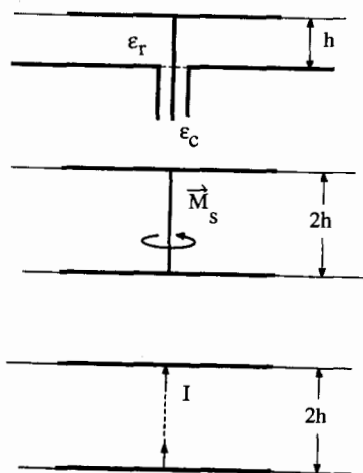


**Fig. 8.17** Microstrip patch antenna excited by a coaxial probe  
The most rigorous model of this configuration considers the probe as belonging to the patch and the whole structure excited by a frill of magnetic current. Simpler models reduce the coaxial line to a filamentary current entering the patch.

The most accurate treatment of a coaxial probe [32, 33] assumes that the portion of the inner coaxial conductor embedded in the substrate belongs to the patch. The whole structure is then excited by a frill of magnetic current existing

between the inner and outer conductors of the coaxial line on the ground plane (Fig. 8.17). For thin substrates, however, replacing the coaxial probe by a vertical filament of current gives results accurate enough for engineering purposes.

If the Galerkin technique is used, we can model the probe as a filament of zero diameter ending in a point charge at the junction with the patch. The calculation of the excitation fields would normally require a knowledge of the fields created by vertical electric dipoles embedded in the substrate; however, the reciprocity theorem allows the evaluation of the terms  $b_i$  (eqn. 8.106) using only formulas related to horizontal electric dipoles. Thus, we have

$$b_i = \int_{S_0} f_i \cdot E^e ds = \int_{V_e} J^e \cdot E_i dv \quad (8.108)$$

where  $E_i$  is the field created by the surface current density  $J_s = f_i$  of eqn. 8.99 and  $E^e$  is the field produced by the excitation current density  $J^e$  [A/m<sup>2</sup>] entering the feed point  $(x_e, y_e)$ . The total excitation current is normalised to 1A, i.e.

$$J^e = e_z \delta(x - x_e) \delta(y - y_e) \quad -h < z < 0 \quad (8.109)$$

and its domain  $V_e$  reduces to a segment of length  $h$  in the case of zero-diameter filament. Consequently:

$$b_i = \int_{-h}^0 E_i \cdot e_z dz \quad (8.110)$$

Finally, in terms of the Green's functions we have

$$b_i = - \int_{S_0} G_0(r_e|r') h_i ds' - j\omega \int_{S_0} e_z \cdot \int_{S_0} \bar{G}_A(r_e|r') \cdot f_i ds' \quad (8.111)$$

an expression which can be cast in an easier form as

$$b_i = - \int_{S_0} G_v^*(r_e|r') h_i ds' \quad (8.112)$$

with the modified scalar Green's function being given by

$$G_v^* = u_0 \tanh uh / u D_{TM}.$$

Now, once the vector of excitation terms  $b = (b_i)$  is known, the amplitudes of the basis functions are obtained by solving the linear system of equations (eqn. 8.104). The input impedance is finally given by

$$Z_{IN} = - \sum_i \alpha_i \int_{-h}^0 E_i(r_e) \cdot e_z dz = -b \cdot C^{-1} \cdot b \quad (8.113)$$

When the subsectional basis functions are used together with razor test functions, the coaxial probe must be modelled more carefully in order to avoid mathematical singularities in the excitation terms. The total current entering the probe must be spread over a region of the patch surrounding the insertion point. A simplified attachment mode in which the current is spread over a cell with a linear dependence has been developed and successfully tested [38]. In the frame-

work of this model, the expression 8.108 for the excitation terms is still valid but the excitation  $E^e$  is created by the currents belonging to the probe and to the attachment mode. Also, the expression 8.113 for the input impedance can still be used, but the effect of the attachment mode on itself must be added in order to obtain accurate predictions for the reactance values. Finally, owing to the discretisation inherent in this approach, the excitation point  $(x_e, y_e)$  can only be located at the centre of a charge cell.

*The reactance of the probe:* Expression 8.113 gives the impedance at the patch level, i.e.  $z = 0$ . To obtain the impedance at the ground plane level,  $z = -h$ , we need to add in series the self-impedance of the coaxial probe. Assuming now that the inner conductor of radius  $r_c$  carries a current  $I$  evenly distributed on its surface, we have

$$J_z = e_z \frac{I}{2\pi r_c} \quad (8.114)$$

For thin substrates, we can approximate the magnetic potential due to these currents by

$$A_z = \frac{\mu_0}{4\pi} \frac{1 - jk_0|\mathbf{r} - \mathbf{r}'|}{|\mathbf{r} - \mathbf{r}'|} \quad (8.115)$$

and the self impedance is given by

$$Z_{\text{coax}} = 60 \left[ (k_0 h)^2 \sqrt{\epsilon_r} + jk_0 h \arcsin \frac{2h}{r_c} + \frac{r_c - \sqrt{r_c^2 + 4h^2}}{2h} \right] \text{ ohms} \quad (8.116)$$

This term is mainly inductive. Thus, finally, a better estimate of the input impedance of a coaxial-fed antenna is

$$Z_{\text{in}} = \text{eqn. 8.113} + Z_{\text{coax}} \quad (8.117)$$

### 8.7.3 Multiport analysis

In many practical situations the microstrip antenna is excited simultaneously at  $M$  points, for instance, in the case of a microstrip array. In this case the antenna can be considered as an  $M$ -port device and standard circuit theory may be applied to completely characterize the antenna.

The first step is to solve the linear system  $C\alpha = b$ , obtained by application of the method of moments,  $M$  times for  $M$  different excitation vectors  $b_i$ . These vectors correspond to a physical situation in which a unit current is entering the  $j$ th port while the remaining  $M-1$  ports are open-circuited. After solving the matrix equation, we get the vector  $\alpha_j = C^{-1}b_j$  containing the amplitudes of the  $N$  basis functions. Then, by computing the voltage at each port we get the quantities  $Z_{ij}$ ,  $i = 1, 2, \dots, M$ , which is the  $j$ th column of the impedance matrix

of the  $M$ -port. Therefore, the complete determination of the impedance matrix requires the solution of  $M$  linear systems, but, fortunately, the matrix  $C$  of the system remains unchanged when exciting each port.

The elements  $Z_{ij}$  have been termed 'input impedances' previously (eqns. 8.113 and 8.117); however, it must be pointed out that these are input impedances corresponding to a single-port excitation since the remaining  $M-1$  ports are open-circuited. These impedances may be quite different from the true input impedances for which an expression will be given now.

Let us consider that each port is connected to a voltage generator  $U_i$  with an internal impedance  $Z_{Li}$  (Fig. 8.18). This arrangement includes the case of a passive load  $Z_{Li}$  by allowing  $U_i = 0$ .

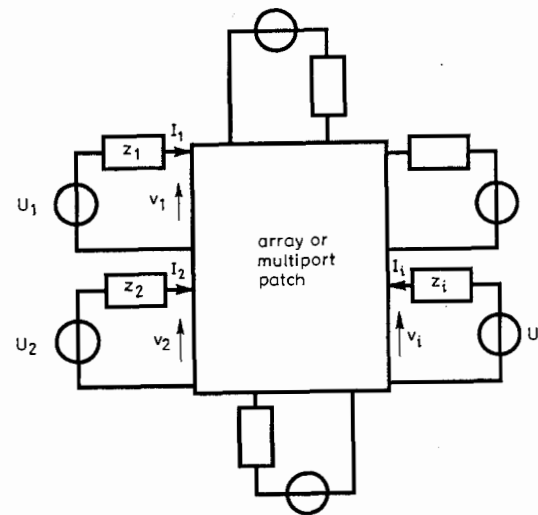


Fig. 8.18 Equivalent circuit of a microstrip antenna array considered as a multiport device. The voltage generators are replaced by short circuits at the ports terminated with a passive load

We define a vector  $U$  with elements  $U_i$  and a diagonal load matrix  $Z_L$  with elements  $Z_{Li}$ . The equations relating currents  $I_i$  and voltages  $V_i$  at each port (Fig. 8.18) are

$$U = Z_L I + V = (Z_L + Z)I \quad (8.118)$$

where  $Z$  is the matrix of impedances previously calculated. The vector of port currents is then given by

$$I = (Z_L + Z)^{-1} U \quad (8.119)$$

and the vector of port voltages is  $V = Z(Z_L + Z)^{-1}U$ . The new vector

$$\alpha^* = \sum_{i=1}^N I_i \alpha_i \quad (8.120)$$

contains the amplitudes of the basis functions for the real working conditions of the antenna, i.e., with all the loads and excitations simultaneously present. This is the vector to be used in the computations of the radiation pattern and when studying the surface current distribution. Finally, the input impedance at each port is

$$Z_{IN|port i} = \frac{V_i}{I_i} = \frac{Z(Z_L + Z)^{-1}U_i}{(Z_L + Z)^{-1}U_i} \quad (8.121)$$

It is clear that, for a single-port antenna, this input impedance equals the parameter  $Z_{11}$  which is directly given by eqns. 8.113 or 8.117.

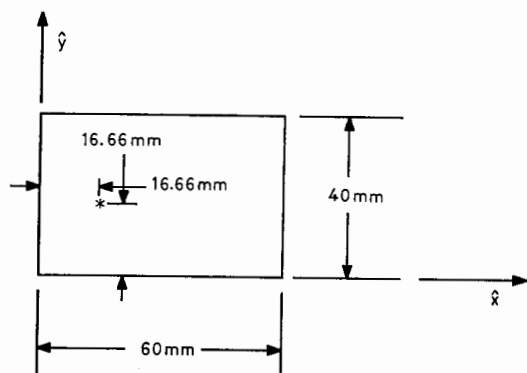


Fig. 8.19 Geometry of a single rectangular patch

$$\epsilon_r = 2.55 \quad \tan \delta = 0.002$$

$$h = 1.28 \text{ mm} \quad Z_0 = 0.9e-7$$

### 8.8 Single rectangular patch antenna

In previous Sections the mathematical theory and numerical procedures have been developed for the analysis of general microstrip structures. This Section will concentrate on a single, rectangular, coaxial-fed patch to illustrate how the theory is applied, present computed results for a simple common structure and answer some of the questions that remain. Remaining questions include the convergence of the method-of-moments procedure and the advantages and disadvantages of the various choices of basis functions presented in Section 8.6. Results will be presented for a single patch as shown in Fig. 8.19 showing the

input-impedance loci on the Smith chart, the surface current distribution at several resonances and the far-field radiation pattern.

#### 8.8.1 Entire-domain versus subdomain basis functions

Section 8.6 presented several choices of basis functions that could be used in a MoM procedure. Among the choices were wide-triangle or rooftop subdomain basis functions used with razor testing and entire-domain cosine basis functions used in a Galerkin procedure, i.e. tested with cosine testing functions. Computer programs have been written using these two choices of basis and testing functions, and a comparison of the results obtained will be presented in this Section.

The calculation of the far-field radiation pattern will be considered first. If subdomain basis functions are used the patch is reduced to an array of horizontal electric dipoles (HED). In this sense, each rooftop basis function is equivalent to a HED whose moment is given by the product of the total current flowing across the common border of two cells times the distance between the centres of the cells.

Now, the far field for a horizontal dipole, which can be thought of as the element pattern in this procedure, is multiplied by the array factor resulting from the segmentation of the patch to give the total far field pattern. Mathematically, the far field is thus given by

$$E_\alpha = G_E^{\alpha x}(r|\theta) \sum_{i=1}^M a I_{xi} \exp(jk_0 e_r \cdot q_i') + G_E^{\alpha y}(r|\theta) \sum_{j=1}^N b I_{yj} \exp(jk_0 e_r \cdot q_j') \quad (8.122)$$

where  $\alpha = \theta, \varphi$ ,  $I_{xi}$  and  $I_{yj}$  are the MoM current coefficients and  $G_E$  represents the far fields due to a HED. The pattern can then be integrated to calculate the directivity, gain and efficiency.

When properly chosen entire domain basis functions are used, the far field for each basis function can be calculated analytically, and the total far field is a simple sum of the fields generated by each basis function. For other choices of basis functions costly numerical integration techniques may be required. Fig. 8.20 shows the far-field pattern for a single rectangular patch. The subdomain rooftop and entire-domain cosine basis functions yield identical co-polar patterns at resonance while only the rooftop basis functions yield an estimate of the cross-polar pattern. The cross-polar pattern is due mostly to currents on the patch in phase with the excitation spreading out from the coaxial probe, and to the currents in the probe. In general, the cross-polarised pattern is very difficult to calculate accurately and is sensitive in practice to the size of the ground plane; an item not included in the numerical model. The model can be used, however, to study the effect of the placement of the coaxial probe on the cross-polar pattern. Figs. 8.20a and 8.20b show the far-field pattern of a single patch when excited by a coaxial probe located at different points.

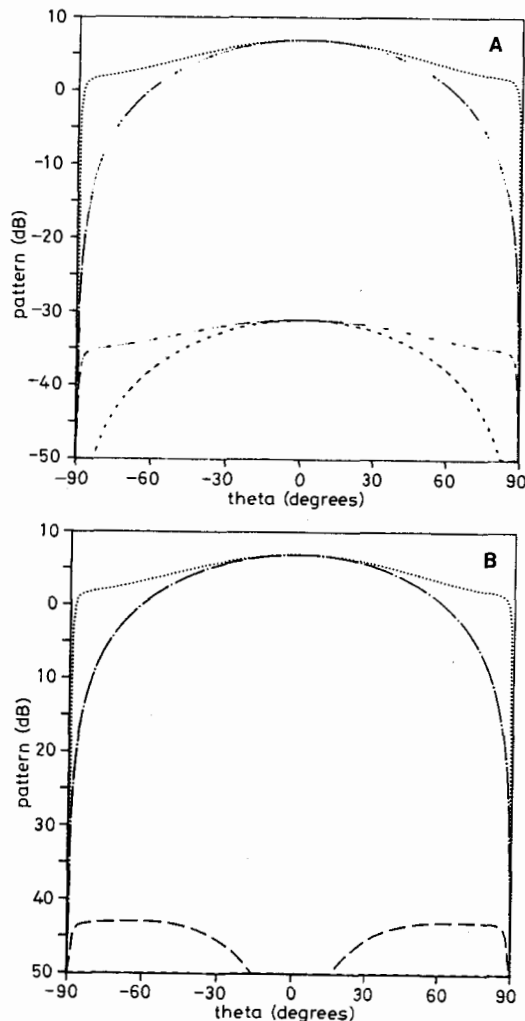


**Fig. 8.20** Radiation pattern for the single rectangular patch shown in Fig. 8.19. Frequency = 1.565 GHz.

- A Coaxial feed at  $x = 16.66$  mm,  $y = 16.66$  mm  
 B Coaxial feed at  $x = 16.66$  mm,  $y = 20$  mm  
 ..... E-plane co-polar  
 ----- H-plane co-polar  
 -.-.- E-plane cross-polar  
 --- H-plane cross-polar

The entire domain functions could, in theory, model accurately the patch at frequencies away from resonance and its cross-polar behaviour, however, in practice, this is costly. Near resonance only one or two entire domain functions are needed to model surface current, and are therefore very well suited to standard geometries near resonance. The cost to include additional basis functions needed away from resonance or to calculate the cross-polar pattern is, however, relatively high compared to the subdomain basis functions. Thus it may be more efficient to use subdomain basis functions when studying a single patch or small array away from resonance or when cross-polar pattern is needed.

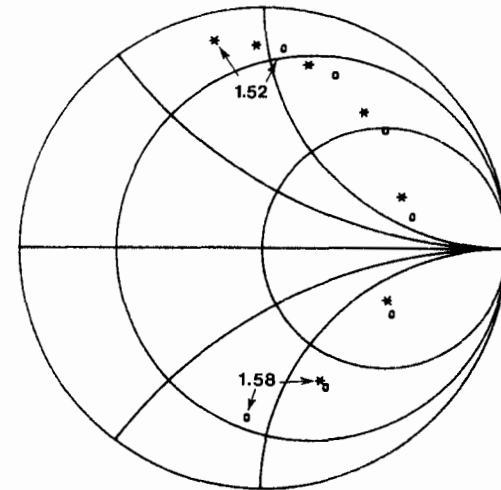


**Fig. 8.21** Input impedance for the single rectangular patch shown in Fig. 8.19.

- Frequency range: 1.52–1.58 GHz.  
 Frequency increases clockwise with a 0.01 GHz step  
 \* Rooftop basis functions  
 ○ Entire-domain cosine basis functions

The input impedance for a single patch is given on the Smith chart of Fig. 8.21. The two choices of basis functions yield approximately the same results with a slight shift in frequency. The resonant frequencies obtained differ by 0.77%, which is often much less than what arises due to uncertainties in the manufacturing process and material parameters. Fig. 8.22 shows the variation of the real part of the input impedance as a function of position for three choices of width/aspect ratios. In each case, the coaxial line was centered in the non-resonant direction on the patch and then moved inward from the edge of the patch to the centre. Note that the results were calculated at the resonant frequency for each patch.



## 8.8.2 Convergence using subsectional basis functions

The question of convergence must always be dealt with when using a moment method. If a numerical result has not converged there is virtually no hope of its being correct. The factors affecting convergence include: the choice of basis and testing functions, frequency, antenna shape, the dielectric used and even the numerical precision of the computer. Since this list includes nearly all the parameters of the antenna and affects nearly all of the decisions made during the development of the computer program to some degree, it is difficult to give rules that guarantee that a particular result has converged. However, several rules of thumb are applicable and can be used as a base when studying convergence. This Section will briefly demonstrate how the MoM solution using subsectional basis functions converges.

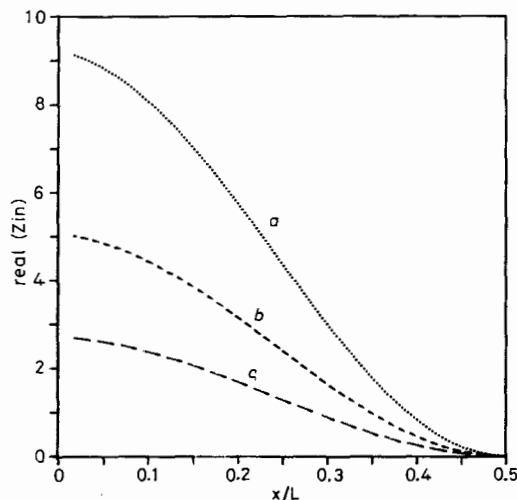


Fig. 8.22 Real part of the input impedance as a function of the position on the patch. The coaxial is centered along the non-resonant direction and moved from the edge of the patch ( $x/L = 0$ ) to the centre of the patch ( $x/L = 0.5$ ).

For case (a) the antenna parameters are given in Fig. 8.19 where  $L = 60$  mm and  $W = 40$  mm. For cases (b) and (c) the width  $W$  is varied.

- (a)  $\cdots \cdots L/W = 1.5$   $f_{\text{resonance}} = 1.555$  GHz  
 (b)  $----- L/W = 1.0$   $f_{\text{resonance}} = 1.543$  GHz  
 (c)  $- - - - L/W = 0.667$   $f_{\text{resonance}} = 1.535$  GHz

The general rule of thumb given in the published literature is that, when using subsectional basis functions, of the order of 10 basis functions per wavelength are needed to obtain good results. This rule also holds for microstrip antennas operating near the first few resonances when calculating the input impedance. It is interesting to note, though, that the number of basis functions in the

direction transverse to the resonance direction, i.e. parallel to the H plane at the first resonant frequency, may be reduced without a significant penalty, resulting in large savings in computation time. Fig. 8.23 shows how the input impedance of a rectangular patch converges when the number of basis functions in the H-plane direction is varied at frequencies near the first resonance. Note the resonant frequency changes by only 0.3% when using three basis functions in the transverse direction as opposed to using 7, however, the input impedance changes by approximately 20%. Thus, a rough study of the antenna's resonant frequency and radiation pattern can be performed quickly at low cost. The final analysis can then be performed using additional basis functions.

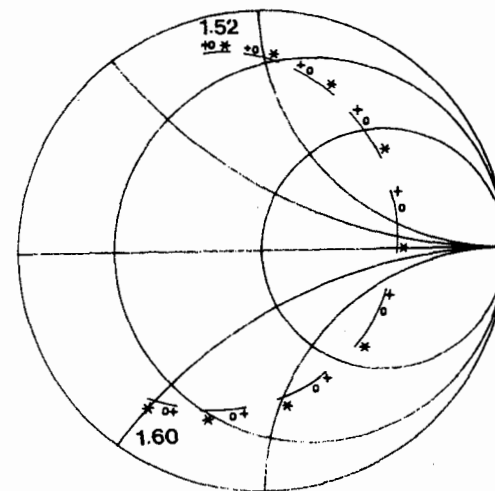


Fig. 8.23 Input impedance for the single rectangular patch shown in Fig. 8.19 with the coaxial centered vertically ( $y = 20$  mm) and at  $x = 16.66$  mm versus the number of basis functions in the H-plane direction, i.e. along the y-axis

Frequency range is from 1.52 GHz increasing clockwise to 1.60 GHz with a step of 0.01 GHz

+: 9 by 7 cells

0: 9 by 5 cells

\*: 9 by 3 cells

## 8.8.3 Surface currents

The subsectional basis functions can be used to model virtually any current distribution owing to their flexibility. As an example, a rectangular patch was analysed and measured at the first four resonances,  $TM_{100}$ ,  $TM_{010}$ ,  $TM_{110}$  and  $TM_{200}$ . The patch dimensions are  $60 \times 40$  mm and the dielectric is a standard low-frequency printed-circuit substrate with high losses in the microwave range ( $\epsilon_r = 4.34$  and  $\tan \delta \approx 0.02$ ). The excitation point has been selected at

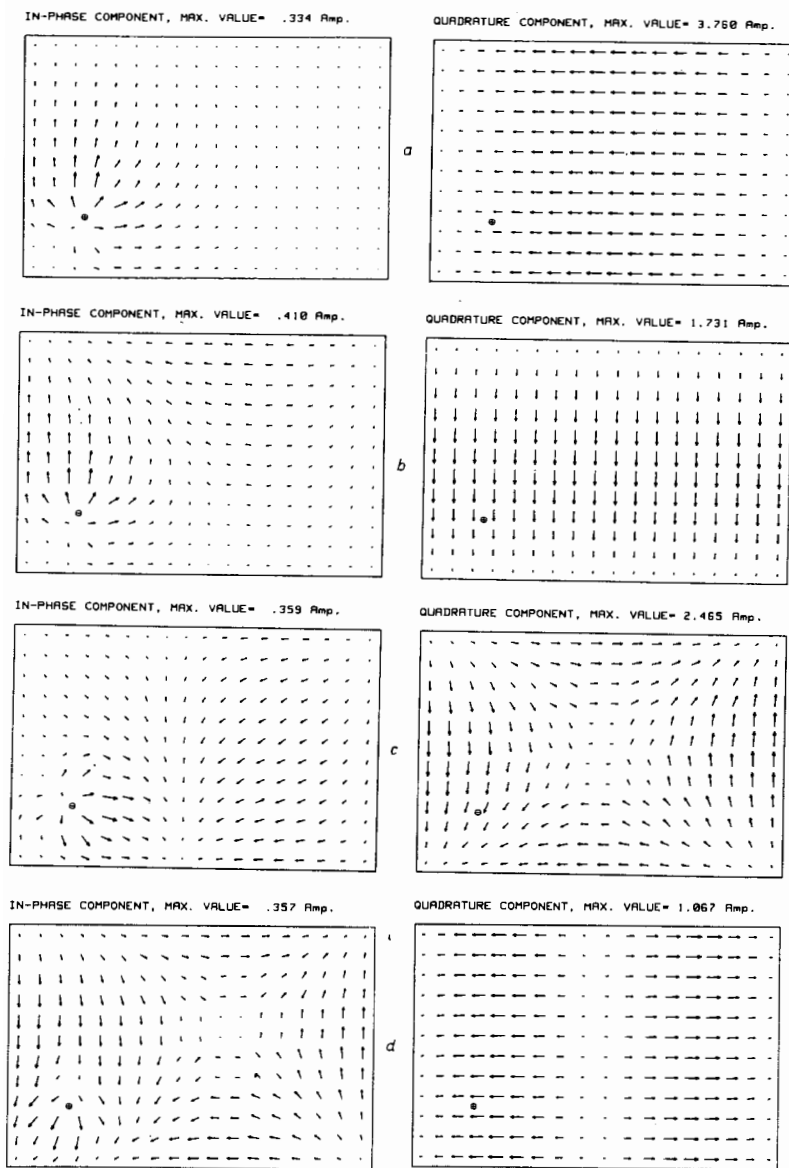


Fig. 8.24 In-phase and quadrature-phase current distributions for a rectangular patch ( $60 \times 40$  mm,  $h = 0.8$  mm,  $\epsilon_r = 4.34$ ,  $\tan \delta = 0.02$ ). After [38].

- (a)  $TM_{100}$  mode; frequency = 1.206 GHz  
 (b)  $TM_{010}$  mode; frequency = 1.783 GHz  
 (c)  $TM_{110}$  mode; frequency = 2.177 GHz  
 (d)  $TM_{200}$  mode; frequency = 2.405 GHz

$x = y = 10$  mm (taking a corner as origin of co-ordinates). This location provides reasonable impedance levels for the first four resonances. The theoretical predictions for the resonant frequencies were, respectively, 1.206, 1.783, 2.177 and 2.405 GHz. The accuracy of these results, when compared with measurements, was always better than 1%.

Fig. 8.24 shows the current distribution calculated using  $(9 \times 6)$  subsectional basis functions. For each resonance, two plots give the real and the imaginary part of the currents, respectively, in phase and out of phase (in quadrature) with the coaxial excitation. The numerical values given in each Figure correspond to the peak value of the current (longest arrow). The imaginary parts of the current are dominant at resonance and their peak value can be many times greater than the unit current used as excitation. The distribution of the imaginary part is independent of the coaxial position and follows closely the shape of the eigen modes of the equivalent cavity. On the other hand, there is a real part whose peak value is always less than unity and whose distribution is mainly controlled by the position of the excitation.

These results justify the use of entire-domain basis functions as a first approximation of the true current distribution. However, an entire-domain basis cannot account for the part of the current depending directly on the excitation (the real part). Therefore, the input impedance values will not be very accurate for weak resonances, and predictions for cross-polar radiation will fail for the patch. However if the impedance level is high, a single entire-domain basis function will yield engineering accuracy at the first few resonances where the antenna is most likely to be operated.

Fig. 8.25 gives the measured and computed values of the input impedance for the two first resonances. Good agreement is observed in each case.

## 8.9 Microstrip arrays

Microstrip patch antennas are inherently low-gain antennas and this fact partially offsets the advantages they offer in terms of cost and ease of fabrication. However, microstrip patch antennas are particularly well suited from a technological point of view to be grouped in large arrays to obtain high gain. Typically, the feed lines are integrated on the same substrate. It may also be possible to integrate active devices for phase shifters and pre-amplifiers on the same substrate, or on a lower layer supporting the active elements that has a different permittivity better suited to the active elements. An integrated array constructed in this manner is compact, light weight and reliable. This Section will be concerned not with the feed network or the active elements but with the actual array of microstrip patch antennas and how the numerical techniques presented in the previous Sections can be applied to the study of arrays.

Antennas at the heart of an array interact among one another, often in a manner that degrades the overall array performance. Each active antenna

induces currents in its neighbours affecting the element's radiation pattern and input impedance. Thus, elements in an array environment have to be studied in the actual array environment to properly account for mutual coupling [34, 35]. However, when the coupling between array elements is less than 20 or 30 dB, it may be possible to neglect mutual coupling and still obtain acceptable results.

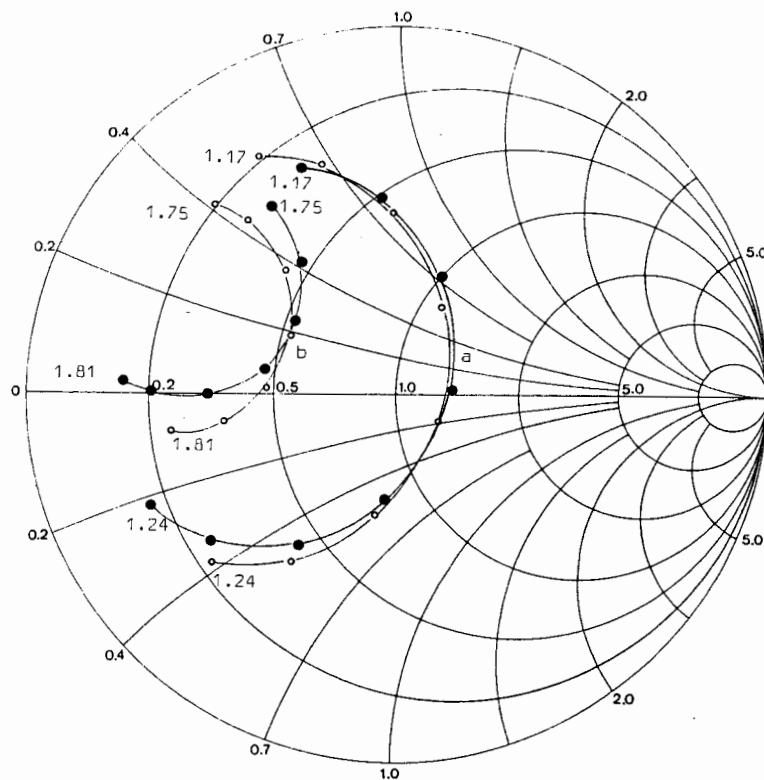


Fig. 8.25 Input impedance near the two first resonances of the patch of Fig. 8.24. After [38].  
○ Theory ( $9 \times 6$  cells)  
● Measurements.

This section will present results for several small arrays and show how the element factor and input impedance are affected when an isolated element is incorporated in an array.

### 8.9.1 Array modelling

To accurately model an array the model should not assume any particular

current distribution on the elements. The method of moments is well suited for the task because any current distribution can be calculated to the desired precision and coupling coefficients are easily calculated. However, practical limitations exist when applying the MoM to anything but small arrays. The use of subsectional basis functions, while very flexible in modelling arbitrary geometries and current distributions, comes with a high price in the number of unknowns. To accurately model an element of the array approximately 50 unknowns are needed; thus for a linear array 10 elements long, 500 unknowns are needed. It can be seen that the capacity of even the largest currently available computer is quickly surpassed.

There are, however, several techniques that can be used to study larger arrays without simply using a larger computer or more computer time. These techniques include:

- (a) Entire domain basis functions
- (b) Infinite array techniques

Additionally, specialised numerical techniques may be applied with success in certain cases. The method of conjugate gradients has been proposed as a method that would allow the solution of larger systems of linear equations [36, 37]. However, normally the MoM matrix is not sparse and the slow convergence of iterative routines applied to fully populated linear systems precludes their use.

Of the two techniques discussed above only the use of entire-domain basis functions will be discussed since infinite array techniques are included as a full Chapter of this handbook. Using entire-domain basis function only one or two basis functions are typically needed at resonance per element; so arrays having up to several hundred elements can be studied easily with today's computers. However, the study of circularly polarised elements or the cross-polarised fields requires the use of additional higher-order basis functions. This considerably increases the computation time and reduces the size of largest array that can be studied.

### 8.9.2 Mutual coupling

A  $2 \times 2$  element array was build on a lossy, inexpensive substrate and the four elements of the scattering matrix were measured and compared with the results obtained using the numerical procedures presented previously in this Chapter. The scattering matrix is defined by

$$S = (Z - I)(Z + I)^{-1} \quad (8.123)$$

where  $Z$  is the impedance matrix with elements calculated using eqn. 8.117 and  $I$  is the unit dyadic.

The array consisted of four identical patches, each 60 mm along the  $E$ -plane and 40 mm along  $H$ -plane. The substrate thickness was 0.8 mm and the dielectric constant was 4.34 with a loss tangent of 0.02. The elements were coaxially fed with the coaxial line centered along the  $H$ -plane and located 10 mm from the

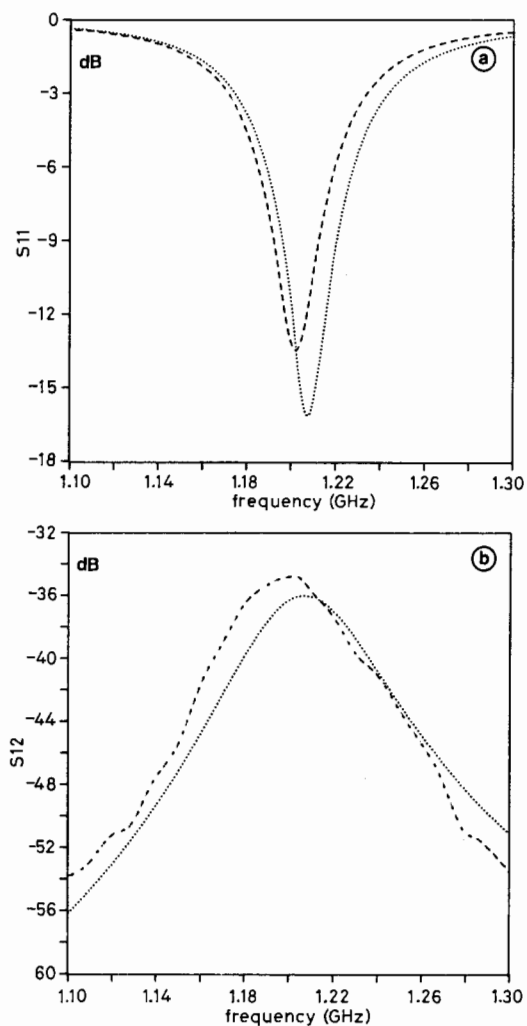


Fig. 8.28 Scattering parameters for a  $2 \times 2$  microstrip array: measured versus theory

Patch size: 60 mm by 40 mm,  $h = 0.8$  mm

$\epsilon_r = 4.34$   $\tan \delta = 0.02$

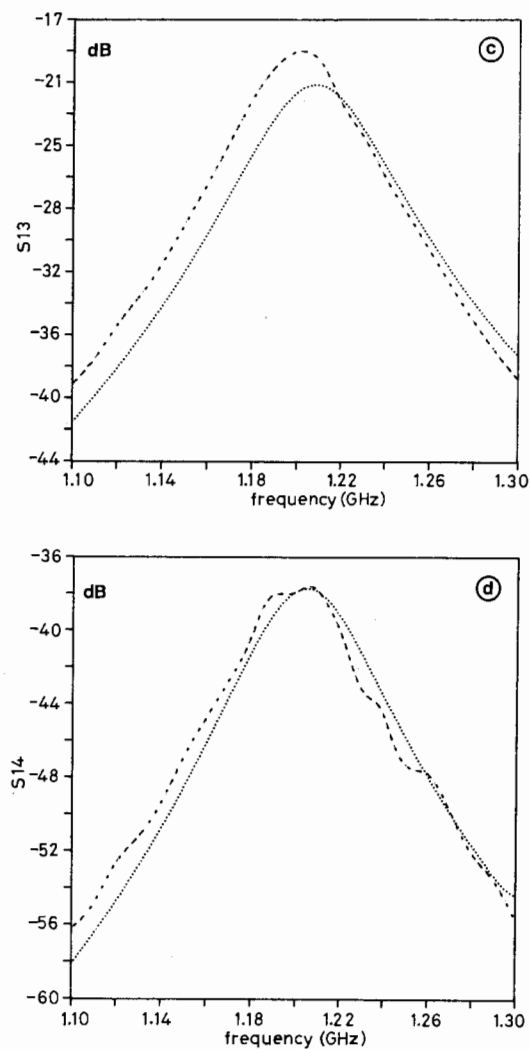
E-plane separation 20 mm between patch edges

H-plane separation 16 mm between patch edges

(a)  $S_{11}$  (b)  $S_{12}$

(c)  $S_{13}$  (d)  $S_{14}$

---- Measured ..... Theory



edge. The separation between the patches was 20 mm along the  $E$ -plane and 16 mm along the  $H$ -plane, corresponding, respectively, to 0.08 and 0.064 free-space wavelengths at the isolated patch's resonance of 1.2 GHz. The results are shown in Fig. 8.26. The two algorithms, which use different basis functions, yield nearly identical results across the frequency band. As can be seen, the agreement between the measured and calculated results is good.

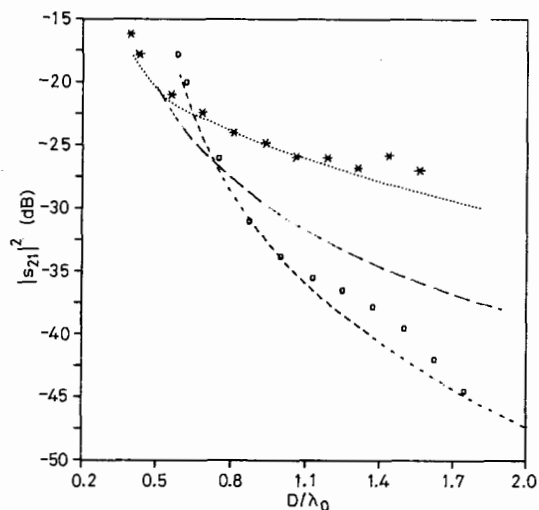


Fig. 8.27 Measured (Jedlicka, Poe and Carver [35]) and calculated mutual coupling between two coaxial-fed microstrip antennas versus the separation between the patch centres  $D$  measured in free-space wavelengths

$W = 105.7$  mm  $L = 65.5$  mm  $h = 1.6$  mm  
 $\epsilon_r = 2.53$   $f_r = 1.414$  GHz

■ Measured  $E$ -plane (From Reference 35)  
 ○ Measured  $H$ -plane (From Reference 35)  
 ..... Calculated  $E$ -plane  
 ----- Calculated  $H$ -plane  
 -.-.-.- Calculated  $45^\circ$  plane

Fig. 8.27 gives the  $E$ - and  $H$ -plane coupling results as a function of the distance between two patches measured by Jedlicka, Poe and Carver [35], and compares these results with those calculated using the theory presented above. Entire-domain basis functions were used. In addition, the calculated coupling results between two antennas located along a diagonal are also presented. It is readily apparent that the  $H$ -plane coupling is stronger for small separations.

This is the kind of coupling found in standard microstrip coupled line filters, and it is mainly due to quasi-static terms and to the space wave. However, the

$H$ -plane coupling decreases faster than the  $E$ -plane coupling, which is sustained by the surface wave and becomes dominant for greater separations.

It must be finally pointed out that the values of the coupling ( $s_{21}$  parameter) are dependent on the input impedance ( $z_{11}$  parameter) and are usually given for a couple of patches matched to  $50\Omega$ . The small differences with measurements in Fig. 8.27 can be due to a slight mismatch of the patches.

### 8.9.3 Linear array of four patches

The last example in this Chapter will illustrate, from a theoretical point of view, the relevance of mutual coupling in the computation of input impedances and mutual coupling. The selected configuration is shown in Fig. 8.28 and consists of four rectangular identical patches fed by coaxial probes and working in the lowest-order mode. The substrate parameters are  $h = 0.787$  mm, and  $\epsilon_r = 2.23$ . The patches are coupled by their non-resonant sides ( $H$ -plane coupling) and they are excited uniformly. On the other hand, their spacing is non-uniform in order to obtain a lower first-sidelobe level [39].

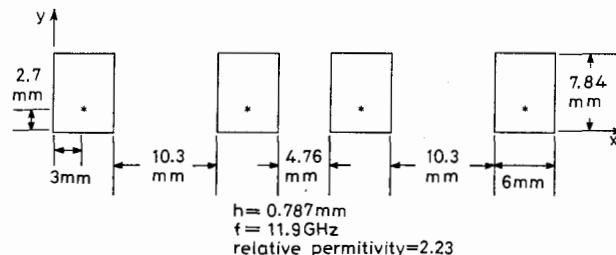
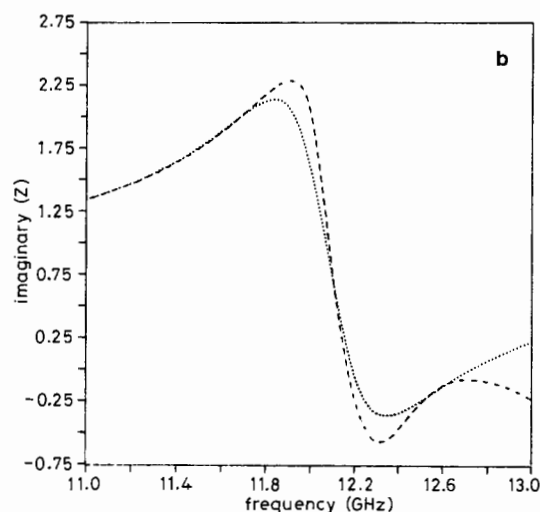
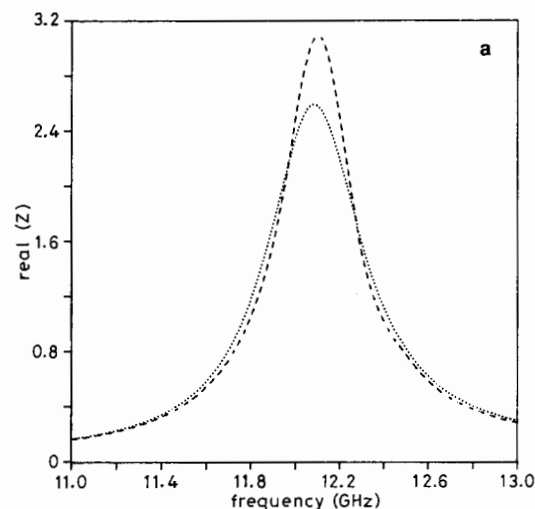


Fig. 8.28 Linear array with four identical patches and nonuniform spacing

The substrate has a permittivity of  $\epsilon_r = 2.23$  and a thickness of  $h = 0.787$  mm. The nominal resonant frequency is  $f_0 = 11.9$  GHz.

Fig. 8.29 shows the normalised real and imaginary parts of the input impedance presented by an inner patch. For each of the quantities, two curves are given, corresponding to theoretical calculations without mutual coupling (the patch is considered as an isolated element) and with mutual coupling (the patch is embedded in an array environment with the three other patches terminated by  $50\Omega$  loads). It can be seen that, for this array, mutual coupling raises the maximum resistance from  $130\Omega$  to  $154\Omega$ . This significant change (18%) shows clearly that mutual coupling should be taken into account for properly matching a microstrip array.

The influence of mutual coupling on radiation patterns is even stronger. Fig. 8.30 shows the  $H$ -plane radiation patterns of an isolated patch and of an inner patch in an embedded configuration. The asymmetries in the geometrical environment of an inner patch (coupled to two patches on one side but only to one



**Fig. 8.29** Calculated isolated-element and embedded-inner-element input impedance versus frequency for the array of Fig. 8.28. Values are normalised to  $50\Omega$

a Real part

b Imaginary part

..... Isolated element

----- Embedded element

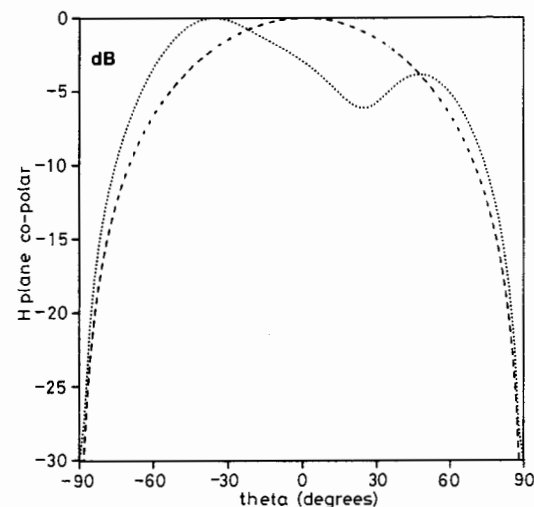


**Fig. 8.30** Calculated isolated-element and embedded-inner-element far-field radiation patterns for the array of Fig. 8.28

In the embedded case all the other elements are loaded with  $50\Omega$

----- Isolated element

..... Embedded element

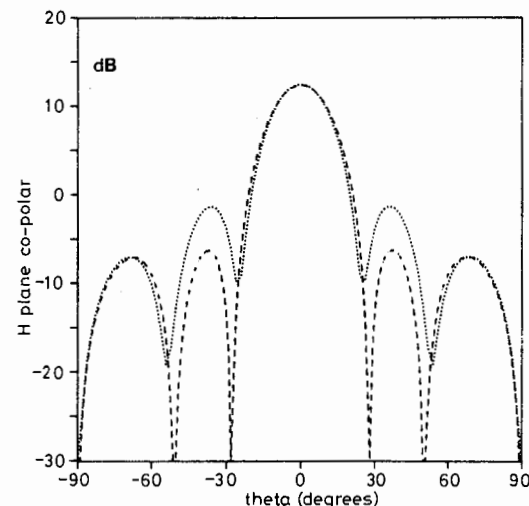


**Fig. 8.31** Calculated H-plane far-field pattern of the array shown in Fig. 8.28 with and without mutual coupling

..... With mutual coupling (MoM result)

First sidelobe = -13.8 dB

----- Without mutual coupling

First sidelobe = -18.6 dB

on the other side) are clearly reflected in the asymmetrical pattern for the embedded situation.

Finally, Fig. 8.31 gives the overall radiation pattern of the array in the  $H$ -plane. A first theoretical prediction neglects mutual coupling and computes the array pattern as the product of the isolated element pattern times the array factor. The first-order sidelobe is then at  $-18.6$  dB, well below the value of  $-13.2$  dB which can be obtained with four equally spaced, uniformly fed elements [40]. However, if the integral-equation model presented in this Chapter is used, mutual coupling is automatically taken into account. Theoretical predictions show then how mutual coupling deteriorates the radiation pattern, raising the first-sidelobe level to only  $-13.8$  dB.

### 8.10 Acknowledgments

The authors would like to thank the members of the Laboratoire d'Electromagnétisme et d'Acoustique (LEMA) for their aid and support. Specifically, Anja Skrivervik, Lionel Barlatey and Bertrand Roudot performed many of the calculations and measurements presented in this Chapter. Also special thanks are due to Mrs. Mary Hall for typing the manuscript.

### 8.11 References

- 1 BAHL, I. J., and BHARTIA, P.: 'Microstrip antennas' (Artech House, 1980).
- 2 STRATTON, J. A.: 'Electromagnetic theory' (McGraw-Hill, NY, 1941).
- 3 MICHALSKI, K. A.: 'On the scalar potential of a point charge associated with a time-harmonic dipole in a layered medium', *IEEE Trans.*, 1988, **AP-36**.
- 4 POGGIO, A. J., and MILLER, E. K.: 'Integral equation solutions of three-dimensional scattering problems', in MITTRA, R. (Ed.), 'Computer Techniques for Electromagnetics' (Pergamon Press, 1973).
- 5 LO, Y. T.: 'Electromagnetic field of a dipole source above a grounded dielectric slab', *J. Appl. Phys.*, 1954, **25**, p. 733.
- 6 BRICK, D. B.: 'The radiation of a Hertzian dipole over a coated conductor', *Proc. IEE*, 1955, **102C**, pp. 103-121.
- 7 BREKHOVSKIKH, L. M.: 'Waves in layered media' (Academic Press, NY, 1960).
- 8 WAIT, J. R.: 'Electromagnetic waves in stratified media', (Pergamon Press, 1962).
- 9 FELSEN, L. B., and MARCUVITZ, N.: 'Radiation scattering of waves', (Prentice Hall, New Jersey, 1973).
- 10 KONG, J. A.: 'Theory of electromagnetic waves', (Wiley, NY, 1975).
- 11 SOMMERFELD, A.: 'Partial differential equations in physics' (Academic Press, NY 1949).
- 12 HARRINGTON, R. F.: 'Time harmonic electromagnetic fields' (McGraw-Hill, NY, 1961).
- 13 MOSIG, J. R., and GARDIOL, F. E.: 'A dynamical radiation model for microstrip structures', in HAWKES, P. (Ed.) 'Advances in electronics and electron physics', (Academic Press, NY, 1982) pp. 139-237.
- 14 MOSIG, J. R., and GARDIOL, F. E.: 'Analytic and numerical techniques in the Green's function treatment of microstrip antennas and scatterers', *IEE Proc.*, 1983, **130H**, pp. 175-182.
- 15 SHASTRY, S. V. K.; Ph.D. Dissertation, Indian Institute of Science, Bangalore, India, 1979.

- 16 UZUNOGLU, N. K., ALEXOPOULOS, N. G., and FIKIORIS, J. G.: 'Radiation properties of microstrip dipoles', *IEEE Trans.*, 1979, **AP-27**, pp. 853-858.
- 17 MOSIG, J. R., and GARDIOL, F. E.: 'Dielectric losses, ohmic losses and surface wave effects in microstrip antennas', Int. URSI Symposium, Santiago de Compostela, Spain, 1983, pp. 425-428.
- 18 MICHALSKI, K. A.: 'On the efficient evaluation of integrals arising in the Sommerfeld halfspace problem', *IEE Proc.*, 1985, **132H**, pp. 312-318.
- 19 LYTLER, R. J., and LAGER, D. L.: 'Numerical evaluation of Sommerfeld integrals'. Report UCRL-52423, Lawrence Livermore Lab., Univ. of California, 1974.
- 20 PANTIS, G.: 'The evaluation of integrals with oscillatory integrands', *J. Comp. Phys.*, 1975, **17**, pp. 229-233.
- 21 BORIS, J. P., and ORAN, E. S.: 'Evaluation of oscillatory integrals', *J. Comp. Phys.*, 1975, **17**, pp. 425-433.
- 22 HURWITZ, H., and ZWEIFEL, P. F.: 'Numerical quadrature of Fourier transform integrals', *Math. Tables Aids Comput.*, 1956, **10**, pp. 140-149.
- 23 ALAYLIOGLU, A., EVANS, G., and HYSLOP, J.: 'The evaluation of oscillatory integrals with infinite limits', *J. Comp. Physics*, 1973, **13**, pp. 433-438.
- 24 SIDI, A.: 'The numerical evaluation of very oscillatory infinite integrals by extrapolation', *Math. Comp.*, 1982, **38**, pp. 517-529.
- 25 HARRINGTON, R. F.: 'Field computation by moment methods' (MacMillan, NY, 1968).
- 26 RAO, S. M., WILTON, D. R., and GLISSON, A. W.: 'Electromagnetic scattering by surfaces of arbitrary shape', *IEEE Trans.*, 1982, **AP-30**, pp. 409-418.
- 27 GLISSON, A. W., and WILTON, D. R.: 'Simple and efficient numerical methods for problems of electromagnetic radiation and scattering from surfaces', *IEEE Trans.*, 1981, **AP-29**, pp. 593-603.
- 28 COLLIN, R. E.: 'Foundations for microwave engineering', (McGraw-Hill, NY, 1966).
- 29 POZAR, D. M.: 'New architectures for millimeter wave phased array antennas', Journées Internationales de Nice sur les Antennes (JINA), Nice, 1986, pp. 168-179.
- 30 KATEHI, P. B., ALEXOPOULOS, N. G.: 'On the modelling of electromagnetic coupled microstrip antennas - The printed strip dipole', *IEEE Trans. Antennas Propagat.*, **AP-32**, pp. 1179-1186, 1984.
- 31 SULLIVAN, P. L. and SCHAUBERT, D. H.: 'Analysis of an aperture coupled microstrip antenna', *IEEE Trans. Antennas Propagat.*, **AP-34**, pp. 977-984, 1986.
- 32 POPOVIC, B. D., DRAGOVIC, M. B., and DJORDJEVIC, A. R.: 'Analysis and synthesis of wire antennas', (Wiley, NY, 1982).
- 33 HALL, R. C., MOSIG, J. R., and GARDIOL, F. E.: 'Analysis of microstrip antenna arrays with thick substrates', 17th European Microwave Conf., Rome, Italy, 1987.
- 34 ALEXOPOULOS, N. G., and RANA, I. E.: 'Mutual impedance computation between printed dipoles', *IEEE Trans.*, 1981 **AP-29**, pp. 106-111.
- 35 JEDLICKA, R. P., POE, M. T., and CARVER, K. R.: 'Measured mutual coupling between microstrip antennas', *IEEE Trans.*, 1981, **AP-29**, pp. 147-149.
- 36 JACOBS, D. A. H.: 'A generalization of the conjugate-gradient method to solve complex systems', *IMAJ of Numerical Analysis*, 1986, **6**, pp. 447-452.
- 37 PETERSON, A. F., and MITTRA, R.: 'Method of conjugate gradients for the numerical solution of large-body electromagnetic scattering problems', *J. Opt. Soc. Am. A*, 1985, **2**, pp. 971-977.
- 38 MOSIG, J. R., and GARDIOL, F. E.: 'General integral equation formulation for microstrip antennas and scatterers', *IEE Proc.*, 1985, **132H**, pp. 424-432.
- 39 GRONAU, G., and WOLFF, I.: 'Spectral domain analysis of microstrip antennas', Proc. of Workshop 'Analytical and numerical techniques for microstrip circuits and antennas', Montreux, Switzerland, March 1988.
- 40 BALANIS, C. A.: 'Antenna theory: analysis and design', (Harper & Row, NY, 1982).